THE ASTROPHYSICAL JOURNAL, 438:932–949, 1995 January 10

EUVE SPECTROSCOPY OF ϵ CANIS MAJORIS (B2 II) FROM 70 TO 730 Å

J. P. CASSINELLI,[1] D. H. COHEN,[1] J. J. MACFARLANE,[1] J. E. DREW,[2] A. E. LYNAS-GRAY,[2] M. G. HOARE,[3] J. V. VALLERGA,[4] B. Y. WELSH,[5] P. W. VEDDER,[4] I. HUBENY,[6] AND T. LANZ[6]

Received 1994 March 31; accepted 1994 July 14

ABSTRACT

We present spectra of the brightest stellar source of extreme ultraviolet (EUV) radiation longward of 400 Å, the B2 II star, ϵ CMa. These data were taken with the three spectrometers aboard the NASA *Extreme Ultraviolet Explorer* satellite (*EUVE*) during the first cycle of pointed observations. We report on our initial studies of the continuum and line spectrum of the stellar photosphere in the 320 to 730 Å region, and on the wind emission lines observed in the 170–375 Å region. This is the first EUV spectrum of an early-type star, and thus makes ϵ CMa the most comprehensively observed B star from the X-ray to infrared regimes.

The radiation in both the H Lyman continuum and He I continuum (shortward of 504 Å) are found to be significantly greater than predicted by both LTE and non-LTE model atmospheres. Since ϵ CMa also exhibits a mid-infrared excess, this points to the outer layers being warmer than the models indicate. The anomalously large Lyman continuum flux, combined with the very low column density measured in the direction toward this star implies that it is the dominant source of hydrogen ionization of the local interstellar medium in the immediate vicinity of the sun. All of the lines predicted to be strong from model atmospheres are present and several wind absorption features are also identified. We have detected emission lines from highly ionized iron, ranging from Fe^{+8} to Fe^{+15}, which arise in the X-ray producing region. The lines are consistent with the *ROSAT* PSPC observations if a multi-temperature emission model is used, and the assumption is made that there is significant absorption beyond that of the neutral phase of the ISM. The EUV spectrum shows a strong He II Lyman-α emission at 304 Å. This line cannot be formed in the upper regions of the photosphere, but rather is due to the recombination of He^{++}, which is itself produced by the X-ray and EUV ($\lambda < 228$ Å) radiation present in the outer atmosphere. The spectrum also shows strong O III 374 Å line emission produced by the Bowen fluorescence mechanism, which has not previously been observed in the spectra of hot stars.

Subject headings: ISM: general — line: identification — stars: atmospheres — stars: early-type — stars: individual (ϵ Canis Majoris) — stars: mass loss

1. INTRODUCTION

Hot stars emit a significant fraction of their radiation in the extreme ultraviolet (EUV) wavelength region from about 100 Å to the hydrogen absorption edge at 912 Å. However, for nearly all early-type stars this radiation can be studied only indirectly through the ionization and thermalization effects inferred from circumstellar emission line nebulae. Initial predictions on the observability of the EUV emission from nearby B stars were made by Cassinelli et al. (1991), MacFarlane et al. (1991), and Kudritzki et al. (1991). The first detections of EUV radiation from early type stars were made with the Wide Field Camera (WFC) on the *ROSAT* satellite (Hoare, Drew, & Denby 1993). The all sky photometric survey made with the *EUVE* satellite (Bowyer & Malina 1991) subsequently discovered that the star ϵ CMa outshines all other nonsolar sources of EUV radiation in the "tin" band from 500 to 740 Å (Vallerga, Vedder, & Welsh 1993). The star is about 30 times brighter in this spectral region than the white dwarf HZ 43, which was previously thought to be the brightest known EUV source. The unexpected discovery that some OB stars have such strong EUV fluxes has important implications for several aspects of hot star research as well as for studies of the interstellar medium.

The B spectral range is an interesting one because of several limits and zones that occur in the HR diagram. The boundary between the O and B stars also marks a sharp difference in the size of H II regions, because the fraction of the stellar radiation in the EUV range depends strongly on stellar temperature for $T_{\rm eff}$ below 30,000 K. Along the main sequence, wind lines are becoming very weak in UV spectra for stars later than B1 V because of the strong dependence of wind driving on luminosity. Along the supergiant spectral sequence there appears a sharp decrease in the wind speed for stars later than B2 Ia because, as explained by Pauldrach & Puls (1990), the winds switch from being driven by strong EUV lines to the more numerous but weaker lines in the UV as the wind becomes optically thick in the EUV continuum. As stellar winds become thinner in the early B spectral region, coupling between the ions and the bulk plasma becomes less efficient and ion runaway accompanied by frictional heating of the wind may occur, reducing the terminal velocity below that expected from theoretical calculations (Springmann & Pauldrach 1992). There are also a variety of interesting classes of stars that lie near the B2 spectral class of ϵ CMa. The emission line Be stars

[1] University of Wisconsin—Madison, Department of Astronomy, 475 North Charter Street, Madison, WI 53706; cassinelli@madraf.astro.wisc.edu; cohen@madraf.astro.wisc.edu.
[2] University of Oxford, Department of Astrophysics, Keble Road, Oxford OX1 3RH, UK.
[3] Max-Planck-Institut für Astronomie, Königstuhl 17, D-69117 Heidelberg, Germany.
[4] Eureka Scientific, 2452 Delmer Street, Oakland, CA 94602.
[5] Space Sciences Laboratory, University of California—Berkeley, Berkeley, CA 94720.
[6] NASA Goddard Space Flight Center, Greenbelt, MD 20771.

TABLE 1

STELLAR PARAMETERS FOR ϵ CANIS MAJORIS

Parameter	Value
Spectral type[a]	B2 II
m_V[a]	1.5
Distance[b]	188 pc
θ_d[c]	0.80 ± 0.05 mas
N_H[d]	0.7 to 1.2×10^{18} cm^{-2}
T_{eff}[e]	$20{,}990 \pm 760$ K
log g[f]	3.2 ± 0.15 cgs
R_*[b,c]	$16.2 \pm 1.2\ R_\odot$
$V \sin i$[g]	35 km s^{-1}

[a] Bright Star Catalog: Hoffleit & Jaschek 1982.
[b] Bohlin et al. 1978.
[c] Hanbury Brown et al. 1974.
[d] This work.
[e] Code et al. 1976.
[f] Hoare et al. 1993.
[g] Uesugi & Fukuda 1982.

peak in number at B2 (V to III). The β Cephei stars are an important class of pulsating stars that also occur in the early B spectral range. So there are many reasons to be interested in new information that can be learned about a star of spectral class B2 from the new spectral band opened by the *EUVE* satellite.

In this paper we report initial results from the first pointed observation of the B2 II MK standard ϵ CMa (Adhara). The star was observed and detected in all three *EUVE* spectrometer bands, with continuum emission seen at wavelengths as low as 320 Å and line emission seen in both the short- and medium-wavelength channels. These first spectroscopic observations of an early-type star below the Lyman edge at 912 Å provide information about the atmosphere, wind, and associated hot plasma.

Some of the known properties of ϵ CMa are listed in Table 1. This object is presently the most comprehensively studied early type star, with observations now in every wavelength band from X-ray to IR. This was one of the few objects for which an angular diameter was determined using the Narrabri optical intensity interferometer (Hanbury Brown, Davis, & Allen 1974). This observation, when combined with observations of the total bolometric luminosity, allow for an empirical determination of the stellar effective temperature. Assuming a distance, the angular diameter measurement leads directly to a determination of the stellar radius. The empirical knowledge of these basic stellar parameters makes ϵ CMa an ideal object for purposes of theoretical modeling.

The paper is organized as follows: In § 2 the calibration of the *EUVE* fluxes and wavelength scale are discussed. Uncertainties in the energy distribution caused by the fixed pattern noise are also estimated. In § 3 the interstellar medium toward ϵ CMa is discussed and we comment on the effect of the ionizing flux from ϵ CMa on the physical state of the local interstellar medium. In § 4 we describe the comparisons with LTE and non-LTE models of the continuum flux, and relate the high Lyman continuum flux to the infrared excess determined from *IRAS* observations. In § 5 we identify many of the absorption features that are present longward of 400 Å. Most of these lines can be attributed to photospheric absorption, although some are attributed to the presence of superionization caused by X-ray photoionization in the stellar wind. In § 6 we discuss the observed emission lines of highly ionized iron that have characteristic temperatures comparable to the temperature range derived from the X-ray observations (Drew, Denby, & Hoare 1994). Strong emission lines of He II to 304 Å and O III at 374 Å are discussed and it is shown that these lines cannot be explained as a result of non-LTE effects in the photosphere of a B star, but instead are the likely result of recombination of He^{++} which has been photionized by the X-ray field. We discuss the production of the 374 Å line as resulting from a resonance pumping of O III by the 304 Å line as occurs in the Bowen mechanism in gaseous nebula. In § 7 the emission line properties are discussed in light of the observations reported in § 6. In § 8 we conclude with a summary of the many challenges presented by the EUV spectrum of ϵ CMa and directions for future work.

2. OBSERVATIONS AND DATA ANALYSIS

Observations of ϵ CMa were awarded by NASA as part of the *EUVE* Guest Investigator program. The star was observed for a total of 186,591 seconds (effective exposure times are listed in Table 2) from 17:45 UT 1993 January 17 to 21:35 UT 1993 January 19 by the three spectrometers on *EUVE* (Bowyer & Malina 1991). These cover the entire EUV range from 70–740 Å. The average spectral resolution across the entire EUV region is $\lambda/\Delta\lambda \sim 250$.

The *EUVE* Guest Observer software package (Version 2.1) was used for reduction and analysis. The data were time filtered using only the nighttime periods of the orbit. Periods of high detector background due to the South Atlantic Anomaly were also removed. Integrated count rates for each spectrometer are given in Table 2.

The source spectra were then extracted from the two-dimensional aspect-corrected images. The average background per wavelength bin was determined from a region directly above and below the spectra and subtracted from the source spectra. The spectra were then divided by the instrument effective areas and corrected for detector deadtime effects using the electronic stimulation pulser which, by pulsing the detector anode once every second, monitors the throughput of the electronics and telemetry. The total deadtime correction applied was 1.078 to the LW spectrum, 1.045 to the MW spectrum, and 1.020 to the SW spectrum. The wavelength and effective area calibration was provided by the *EUVE* Guest Observer Center

TABLE 2

OBSERVATIONAL PARAMETERS

Spectrometer Channel	Spectral Range (Å)	Effective Exposure Time (s)	Count Rate (counts s^{-1})
Short wavelength (SW)	70–183	61,017	$(6.03 \pm 1.67) \times 10^{-3}$
Medium wavelength (MW)	141–373	62,323	$(5.79 \pm 0.24) \times 10^{-2}$
Long wavelength (LW)	289–743	57,287	23.73 ± 0.02

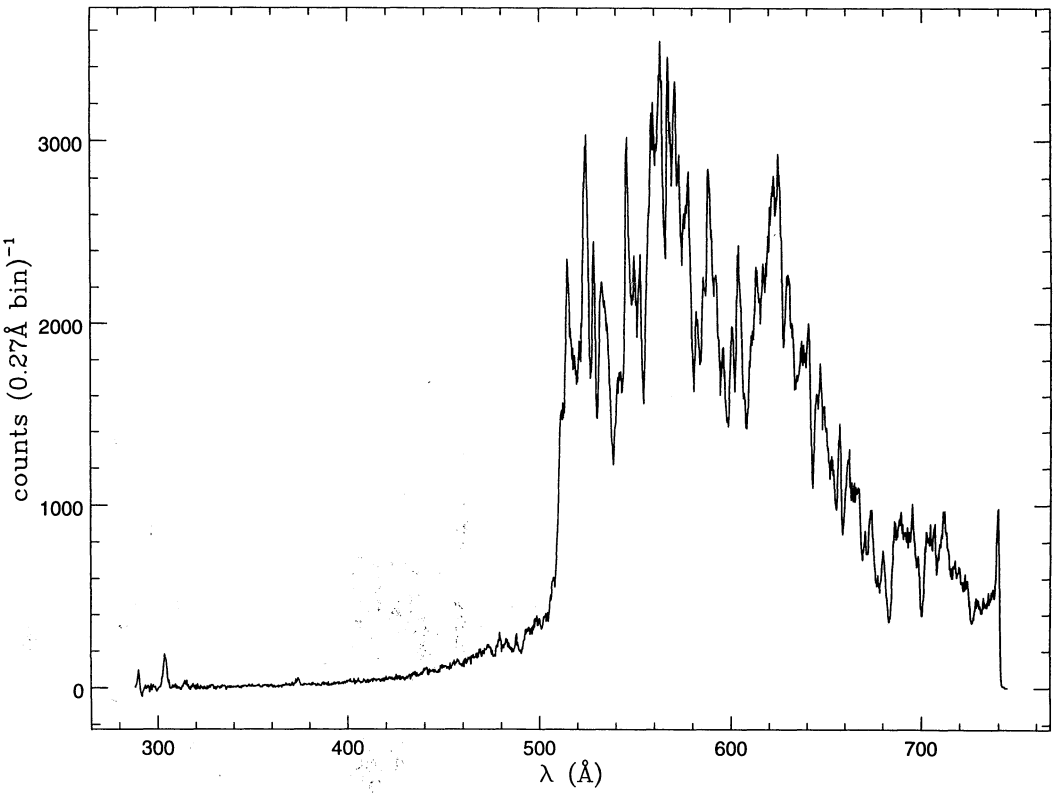

FIG. 1.—ϵ CMa as observed in the *EUVE* LW spectrometer. We display raw total counts per 0.27 Å pixel in an effective exposure time of 57,287 seconds.

(Version 2.1). The wavelength calibration is probably good to within the quoted spectral resolution (FWHM $\lesssim$ 2 Å). The raw LW spectrum is shown in Figure 1.

The intensity errors in the count rate spectra are dominated by statistical variations for wavelengths less than 500 Å and by systematic effects for wavelengths longer than 500 Å where the signal to (statistical) noise ratio is greater than 20 per bin. Errors in the derived absolute density also depend on the effective area calibrations of *EUVE* and await a complete analysis of in-orbit calibration data of many more stars. Assuming the instrument response is unchanged from pre-launch values, the absolute effective areas should be accurate to 25%. The relative response of the three spectrometers can be checked where the wavelength ranges of the three instruments overlap (170 Å to 183 Å for the SW and MW; 290 Å to 373 Å for the MW and LW) and where there is sufficient flux to measure it. The 304 Å He II emission line, detected in both the MW and the LW spectrometers, indicates that the ratio of reported effective areas at this wavelength is accurate to approximately 20%. The higher residual noise in the spectra around the 304 Å spectral line is due to the effects of the increased background from the diffuse resonance scattering of the solar He II emission line from the geocorona. The same effect also occurs at the 584 Å He I emission line but the bright source spectrum dominates at this wavelength.

The dominant systematic error in the flux density for the high S/N spectra is due to the fixed pattern noise in the microchannel plate (MCP) detectors. This effect was known prelaunch (Vallerga, Sigmund, & Vedder 1991) and is due to high spatial frequency distortions at the MCP multifiber boundaries. These distortions cause a periodic variation in the effective size of each pixel, resulting in a spectrally flat continuum spectrum having pseudo-emission and absorption features with semi-amplitudes as large as 10%. This is not a response variation since photon events are not lost, merely shifted slightly in wavelength, such that emission line measurements are unaffected. The effect cannot be corrected after the data have been acquired, since there is no way to generate an EUV flat field in orbit.

3. THE LOCAL INTERSTELLAR MEDIUM TOWARD ϵ CMa

The great intensity of EUV emission observed toward ϵ CMa is primarily due to its position in a Galactic region of very low interstellar hydrogen column density ($N_H \sim 10^{18}$ cm^{-2}), such that there is very little attenuation of the intrinsic EUV stellar flux by the intervening neutral interstellar hydrogen. ϵ CMa lies within a 50 pc diameter, 300 pc long, rarefied interstellar tunnel aligned along the direction toward the star β CMa (Welsh 1991). This elongated interstellar feature appears to be an extension to the Local Bubble region, which is normally considered to asymmetrically surround the Sun to about 50 pc. This tunnel extension, however, has been shown to possess a gas density, n (cm^{-3}), at least 3 to 5 times lower than that normally encountered in the local inerstellar medium (Welsh 1991; Gry, York, & Vidal-Madjar 1985). Our present estimate of the interstellar hydrogen column density toward ϵ CMa results in a neutral gas density of $n < 0.002$ cm^{-3} along the line of sight, thus making this one of the lowest neutral interstellar density regions yet measured.

In Vallerga et al. (1993), it is conjectured that the intense EUV emission from ϵ CMa longward to 500 Å could have an appreciable effect on the ionization balance of the local interstellar gas (within several parsecs of the Sun). Bruhweiler & Cheng (1988) and Cheng & Bruhweiler (1990) have outlined

both the major ionization processes and the contributions from nearby stellar sources to the background EUV radiation field. Their stellar radiation field calculation summed the modeled EUV spectra of the most likely candidates to dominate the EUV field: nearby hot white dwarfs and B stars with low column density. However ϵ CMa was not included in their calculations, due to its distance and spectral type.

Our present observations of the EUV spectrum of ϵ CMa, and the knowledge that the B1 star β CMa is also an appreciable emitter of long wavelength EUV radiation at a level of $\approx$10% of ϵ CMa in the 600 Å bandpass (Hoare et al. 1993; Malina, Marshall, & Antia et al. 1994), clearly indicate that the two nearby B stars make the dominant contribution to the level of photoionization in the local interstellar medium. In fact, the Lyman continuum flux, integrated between 504 and 912 Å, at the Earth as measured from our present *EUVE* spectrum for ϵ CMa alone is 331 photons cm^{-2} s^{-1}. This would give a hydrogen photoionization rate at the Earth, Γ, of 1.1×10^{-15} s^{-1}, a factor of 6 higher than the *total* from all nearby stars predicted by Bruhweiler & Cheng (1988). The implications of this result of the ionization of hydrogen and helium in the solar neighborhood and the local cloud will be discussed in a forthcoming paper.

4. THE PHOTOSPHERIC CONTINUUM EMISSION FROM ϵ CMa

Here we present a comparison between the observed Lyman continuum flux and theoretical energy distributions. We compare the observed flux with that derived from LTE, line-blanketed model atmosphere code ATLAS9 (Kurucz 1992) and from an exploratory non-LTE line-blanketed calculation based on developments of the code TLUSTY (Hubeny 1988; Hubeny & Lanz 1992; with modifications from Hubeny, Hummer, & Lanz 1994 and Hubeny & Lanz 1994). As neither model comes close to providing as much Lyman continuum emission as observed, we go on to an argument exploiting measurements of the mid-IR continuum emission of ϵ CMa that provide insight into the cause of the discrepancy.

Because the angular diameter of ϵ CMa is known (Hanbury Brown et al. 1974; see Table 1) and the star is cool enough to allow direct measurement of practically all of its emitted flux (the Planck maximum falling in the satellite ultraviolet range), its effective temperature is particularly well-constrained. Code et al. (1976) derived $T_{\rm eff} = 20{,}990 \pm 760$ K from the measured angular diameter and the integrated stellar flux longward of 1100 Å, using data from the *OAO 2* satellite and the optical-infrared multicolor photometry of Johnson & Mitchell (1975). An almost identical result was achieved later by Remie & Lamers (1982) based on the related "infrared flux" method of Blackwell & Shallis (1977). Remie & Lamers should have derived an effective temperature $\sim$500 K cooler by virtue of using the fainter ultraviolet flux calibration of Jamar et al. (1976); they did not because they also adopted a nonzero reddening, $E_{B-V} = 0.03$, in place of what is now known to be entirely negligible reddening. We should note that the increased flux that we see in the EUV does not change the effective temperature of ϵ CMa derived from the angular diameter and UV flux observations of Code et al. (1976), because the total EUV flux corresponds to less than 1% of the bolometric flux from the star.

To proceed with a detailed comparison of the *EUVE* spectrum of ϵ CMa with that of a model atmosphere, we must choose a plausible value for the star's surface gravity. We select $\log g = 3.2 \pm 0.15$ on the basis of a distance of 188 pc (Bohlin, Savage, & Drake 1978) and the evolutionary tracks of Maeder & Meynet (1988). This assignment is supported by fits made to published Balmer line profiles (Watson 1972) using profiles synthesized from ATLAS9 model atmospheres via the Balmer line code BALMER9 (as released by R. L. Kurucz).

In Figure 2, we superpose our $T_{\rm eff} = 21{,}000$ K, $\log g = 3.2$ ATLAS9 LTE model atmosphere normalized using the angular diameter (0.8 $\pm$ 0.05 mas, Hanbury Brown et al. 1974) on the *OAO 2* ultraviolet data (Code & Meade 1979) and the multicolor photometry of Johnson & Mitchell (1975). A good fit is obtained at optical and ultraviolet wavelengths. Varying the surface gravity within the state error bounds has little effect at the extremes of the energy distribution. Also shown in the figure is the observed extension of energy distribution of ϵ CMa shortward of the Lyman limit provided by the present *EUVE* observations. The *EUVE* data points have been corrected to remove the effect of interstellar H I absorption, calculated for a column density of $N_{\rm H\,I} = 1 \times 10^{18}$ cm^{-2}. Reasons for this choice of interstellar column are discussed below.

From Figure 2, it is immediately apparent that the LTE model atmosphere flux falls well short of the observed Lyman continuum flux. This is true even if no correction for ISM attenuation is made (i.e., a neutral hydrogen column density of zero still cannot bring the model in line with observations). Is this because the model predicts the wrong temperature structure, or because non-LTE effects are significant, or both?

To determine whether the neglect of non-LTE effects is responsible for the incompatibility, we have used TLUSTY to construct a line-blanketed model ($T_{\rm eff} = 21{,}000$ K, $\log g = 3.2$) in which hydrogen, helium, Fe^{++} and Fe^{+3} are treated in non-LTE. Those ions (Fe^{++} in particular) are the dominant ionization stages of iron for the temperature range of interest. As it is very likely that iron provides most of the metal line opacity, the inclusion of these two iron ions serves to introduce into the model a quite reasonable approximation to the total metal opacity, which in turn allows us to study the effects of non-LTE metal line blanketing on the atmospheric structure quantitatively. The treatment of iron is described in detail by Hubeny & Lanz (1994); in brief, we consider some 23,000 lines of Fe III and 8000 lines of Fe IV—all lines originating between levels with *measured* energies.

The EUV energy distribution predicted by the non-LTE model is compared with that of the LTE model of Figure 3. It is immediately apparent that the non-LTE blanketed (H-He-

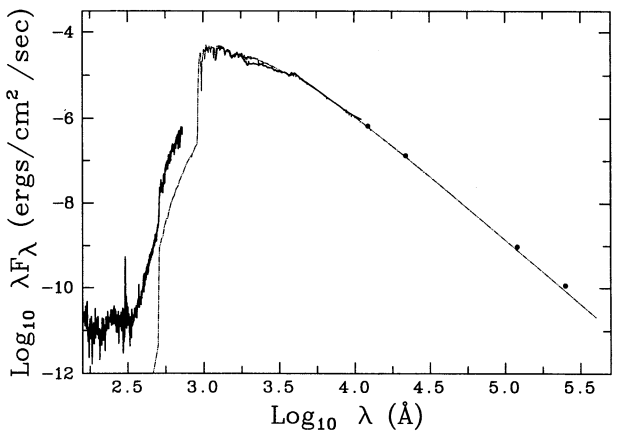

FIG. 2.—Continuous energy distribution of ϵ CMa from far EUV through mid-IR wavelengths, compared with a 21,000 K LTE model.

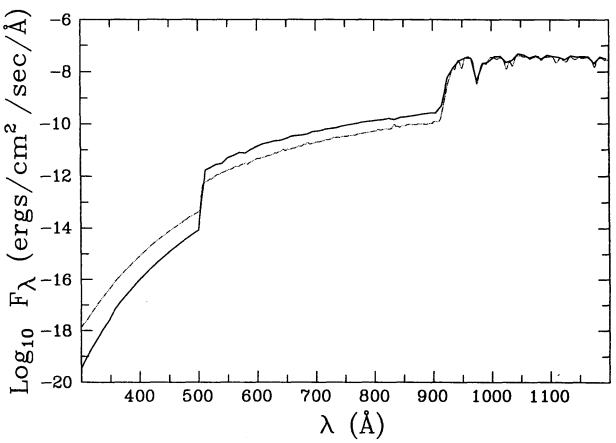

FIG. 3.—Comparison of the flux distribution from the Kurucz model (*solid line*) and the TLUSTY line-blanketed model (*dashed line*) from 300 to 1200 Å.

Fe) model is not the solution to the Lyman continuum flux discrepancy; the main reason being that the ground state of hydrogen is significantly overpopulated with respect to LTE in those layers where the Lyman continuum forms (log $m \simeq -2$, where m is the mass column in g cm^{-2}). Since there is little difference between the temperatures derived in the two models at this depth, and the continuum source function is proportional to $B(\nu, T)/b_1$ (where b_1 is the ground state departure coefficient), the effect of overpopulation in the non-LTE model is inevitably a lowering of the emergent flux with respect to LTE. Thus we find that neither the LTE line-blanketed model, nor the non-LTE iron line-blanketed model, can explain the observed Lyman continuum flux from ϵ CMa.

To gain insight into the cause of the discrepancy between model and observation, we exploit the fact that the Lyman continuum and the mid-infrared continuum form at similar depths within the atmosphere but by different processes. In all the models we have examined (non-LTE with and without line-blanketing, LTE with line-blanketing), the depth of formation of the continuum at $\sim$600 Å has been found to be comparable to that for the 10–15 μm continuum. However, while Lyman continuum emission is extremely temperature-sensitive and subject to non-LTE effects, the mid-infrared source function can be presumed to deviate negligibly from LTE. This is because the dominant opacity sources at these long wavelengths are free-free and bound-free absorption (the latter involving only high-lying bound states). In effect the mid-infrared continuum flux is a thermometer, *quite independent of the details of any model atmosphere calculation*, which tells us the temperature of the zone in the atmosphere in which it forms. Significantly, the reading on the thermometer turns out to be distinctly higher than either the LTE or non-LTE line-blanketed model atmosphere calculations predict. It can be used to estimate the expected intrinsic Lyman continuum emission for the simplest case that departures of hydrogen ground state populations from LTE are modest.

We show the color-corrected 12 and 25 μm fluxes for ϵ CMa from the *IRAS* Point Source Catalog (Version 2, 1988) in Figure 2. They can be seen to lie above the model atmosphere prediction. To derive reliable excesses we compared the non–color-corrected *IRAS* fluxes for ϵ CMa with those of α CMa; placing them on the absolute flux scale of Cohen et al. (1992). This strategy avoids uncertainties in the published *IRAS* zero-point flux calibration and absolute color corrections. We assume that the color corrections and α and ϵ CMa differ negligibly. The data used in this procedure are given in Table 3 together with equivalent blackbody temperatures derived from them. We estimate excesses of 17 $\pm$ 9% and 21 $\pm$ 10% at 12 and 25 μm, respectively. The errors quoted are dominated by *IRAS* measurement accuracy and the uncertainty in the Hanbury Brown et al. (1974) angular diameter. We rule out a significant contribution to these excesses by free-free wind emission because the mass loss rate of ϵ CMa has been estimated very small ($\dot{M} \sim 1 \times 10^{-8}\ M_\odot\ \mathrm{yr}^{-1}$, see Drew et al. 1994, and later sections of this paper).

We have also checked whether the theoretical mid-infrared flux could be underestimated because of inaccuracies in the H I and He II free-free and H I bound-free gaunt factors that are used in the ATLAS9 program. The program uses gaunt factors that have been regarded for many years as definitive and well justified. The largest likely error in the gaunt factors would be caused by interpolations from tables instead of functional fits to the free-free gaunt factors. We have estimated that for our study this could lead to a maximum error in the gaunt factors of 3%, which could increase the theoretical mid-infrared continuum flux by only 0.02 percent at most.

The 12 μm excess of 17 $\pm$ 9% indicates a 16% increase in the temperature of the stellar atmosphere to 16,800 K at the appropriate depth with respect to the Kurucz model. The 25 μm excess yields a temperature indistinguishable from that implied by the excess at 12 μm (see Table 3), suggesting the kinetic temperature is almost constant over the depth range sampled by the 12–25 μm continuum emission (in the model, this range spans a factor of 3 in mass column). Since the temperature-dependence of the opacity in the mid-infrared is not very strong ($\propto T_e^{-3/2}$ for $h\nu \ll kT_e$), the higher temperature

TABLE 3

THE *IRAS* PSC FLUX MEASUREMENTS AND EQUIVALENT BLACKBODY TEMPERATURE

Parameter	$\lambda = 12$ μm	$\lambda = 25$ μm
IRAS PSC non–color-corrected fluxes (Jy):		
α CMa	143.1 $\pm$ 4.3	34.0 $\pm$ 1.7
ϵ CMa	5.6 $\pm$ 0.3	1.36 $\pm$ 0.08
Monochromatic fluxes at the Earth (ergs cm^{-2} s^{-1} Å^{-1}):		
α CMa (Kurucz model)	(1.941 $\pm$ 0.028) $\times$ 10^{-13}	(1.034 $\pm$ 0.015) $\times$ 10^{-14}
ϵ CMa (observed)	(7.60 $\pm$ 0.46) $\times$ 10^{-15}	(4.14 $\pm$ 0.29) $\times$ 10^{-16}
ϵ CMa (Kurucz model)	6.52 $\times$ 10^{-15}	3.43 $\times$ 10^{-16}
Percentage excess	17 $\pm$ 9	21 $\pm$ 10
Equivalent blackbody temperature (K):		
Model prediction	14400	14000
Observed	16700 $\pm$ 1500	16800 $\pm$ 1680

does not imply a significant change in the physical depth of continuum formation with respect to the placement of models predicting cooler outer atmospheres.

Consideration is now given to the effect that raising the temperature to $\sim$17,000 K from $\lesssim$15,000 K (the temperature predicted in the models for the relevant depths) could have on the hydrogen ground state population and hence the depth of the atmospheric layers producing the Lyman continuum emission. Specifically, does the higher than expected temperature invalidate the impression conveyed by the models that the depths of formation of the Lyman and mid-infrared continua are comparable? The change will be greatest if the ground state population responds to temperature changes as in LTE. In practice it is likely that the radiation field created in deeper layers of the atmosphere exerts a significant influence on this population, thus damping its sensitivity to the local temperature. This is reassuring in that model atmosphere theory can be presumed to describe the inner atmospheres of stars such as ϵ CMa rather better than their outer layers. In the worst case—the extreme of LTE—raising the temperature by $\sim$15% moves the depth of formation of the Lyman continuum inward by about a factor of 5 in the mass column [this is deduced from the form of the Lyman continuum opacity's temperature dependence in LTE: $\propto T_e^{-3/2} \exp(h\nu/kT_e)$]. Even this change is not so large that the mid-infrared temperature of $\sim$17,000 K is seriously misleading. Since the kinetic temperature is more likely to increase with depth into the atmosphere rather than decrease, this figure might undershoot the temperature in the Lyman continuum forming layer somewhat (by as much as $\sim$1000 K perhaps).

We now have a temperature to associate with the Lyman continuum forming layers. Provisionally, let it also be assumed that the hydrogen ground state population is close to its LTE value. In this context it is certainly reasonable to assume that the shape of the emergent continuum is similar to that of a blackbody—the continuous opacity changes by less than a factor of 3 over the relevant wavelength range ($\sim$510 Å up to $\sim$720 Å), which defines a quite shallow layer in the atmosphere through which there is unlikely to be a dramatic change of either temperature or hydrogen ground state departure coefficient. However, it also has to be hoped that a conspiracy of very unevenly distributed line-blanketing does not cause us to misconstrue the observed continuum shape. Confirmation that line-blanketing does not severely distort the Lyman continuum awaits a model stellar atmosphere which correctly predicts the observed flux. Noting these caveats, we proceed to identify combinations of intrinsic stellar Lyman continuum emission (blackbodies with $T \gtrsim 17{,}000$ K) and interstellar attenuation (due to neutral hydrogen) that are consistent with the observed energy distribution.

The result of this exercise, carried out as a "dereddening," is shown in Figure 4. By this method we estimate that the interstellar H I column is unlikely to be less than $\sim 7 \times 10^{17}$ cm^{-2}, and probably no greater than $\sim 1.2 \times 10^{18}$ cm^{-2}. Quite plausibly, these limits lie at the lower end of the range, $1.0 \times 10^{18} < N_{\rm H\,I} < 2.2 \times 10^{18}$ cm^{-2} (Gry et al. 1985), set for the slightly more distant star β CMa, believed to be located in the same evacuated interstellar "tunnel" as ϵ CMa (Welsh 1991).

The conclusion to this argument is that a blackbody-like stellar continuum appropriate to the temperature set by an independent probe of the relevant layers in the atmosphere of ϵ CMa (the mid-infrared flux) can be combined with a value for the interstellar column, plausible on independent grounds,

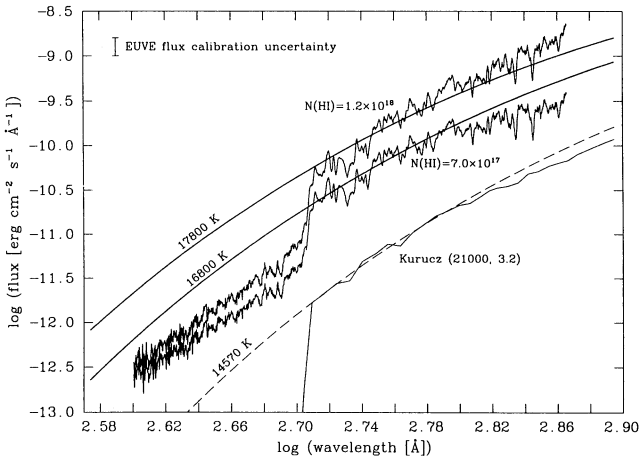

FIG. 4.—Energy distribution of ϵ CMa from 300 to 730 Å after removing the attenuation due to (1) N(H I) = 7×10^{17} cm^{-2}, (2) N(H I) = 1.2×10^{18} cm^{-2}. The correction does not include an estimate of the absorption due to interstellar neutral helium. The "dereddened" energy distributions are compared, respectively, to blackbody curves for 16,800 and 17,800 K. Note that the ATLAS9 LTE line-blanketed model Lyman continuum flux closely follows that of a 14,570 K blackbody. All curves are normalized to the observed angular diameter of ϵ CMa.

to produce an acceptable fit to the measured Lyman continuum emission. Because the mid-infrared continuum measurements demand a temperature of $\sim$17,000 K or more in the layers producing the Lyman continuum flux, fits combining a lower temperature with *under*population of the hydrogen ground state can be ruled out. The possibility of *over*population in consort with a similarly enhanced kinetic temperature remains but, of course, allows an extra free parameter that cannot yet be constrained.

Another important difference between the observed flux distribution and the model predictions is the strikingly shallow "jump" between the H I and He I Lyman continua near 504 Å. In Figure 4, the interstellar correction applied accounted only for H I Lyman continuum absorption. This means that the jump as shown in Figure 4 is over rather than underestimated. The reasoning we have presented regarding the H I Lyman continuum excess applies also to the observed level of the He I Lyman continuum.

There are differences stemming from the very shallow depth of its formation that limit comment at this stage. Firstly, comparison of the excess emission with far-infrared emission from similar, very shallow layers in the atmosphere is not feasible—even ϵ CMa is not bright enough to have been detected longward of $\sim$100 μm! Secondly, non-LTE effects may well play a bigger role in its enhancement. There is also a slight risk this continuum forms in the shallower density gradient of the stellar wind. Finally, it is not clear what ionization correction should be applied in scaling the He I interstellar absorption to that due to H I. To resolve these issues improved model atmosphere calculations are essential.

In summary: ϵ CMa shows a Lyman continuum flux that is over an order of magnitude larger than predicted either by the ATLAS9 or TLUSTY line blanketed models. Because the star also shows an excess of infrared radiation that arises from the Lyman continuum formation region it is concluded that the region is at least 2000 K hotter than expected. Using the temperature estimated from the 12 to 25 μm *IRAS* fluxes, the correction for the interstellar absorption in the 504 to 730 Å region is estimated to be about $1 \times 10^{18}\, N_{\rm H\,I}$ cm^2.

The idea of using a mid-IR excess to infer the presence of an atmospheric temperature enhancement is not a new one. It was concluded by Waters, Cote, & Aumann (1987) that there is a general problem of excess 12 μm emission from OBA stars. However, this was based on comparison with the Kurucz (1979) grid, and the recent study of Cohen et al. (1992) using the newer ATLAS9 grid has shown that this discrepancy has mainly disappeared. In this context, it is of interest that β CMa (B1 II–III) does not exhibit a 12 μm excess, and in addition there are indications from *ROSAT* Wide Field Camera observations of this star that the Lyman continuum flux is also more closely in line with predictions based on the new Kurucz grid (Hoare et al. 1993). *EUVE* spectroscopy of β CMa should soon be available and will allow further investigation of this matter.

5. ABSORPTION LINE IDENTIFICATION

The EUV region is rich in spectral lines from singly to triply ionized stages of abundant elements (Kelly 1987). Our observations of this region show many absorption features, and we make tentative identifications of most of these features using a comprehensive line list assembled by Kurucz. We have used the TLUSTY model and the SYNSPEC program (Hubeny, Lanz, & Jeffery 1994) to predict which lines should be present in a 21,000 K photosphere. The comparison serves several purposes: (a) the model provides an identification of the lines and an estimate of the predicted strengths; (b) because of the large number of lines in the model spectrum, the comparison provides an indication of the degree of overlap of lines, hopefully preventing an overinterpretation of the line profiles; (c) there should be evidence for the wind from ϵ CMa in the EUV spectrum, and it is known from UV studies that wind lines are often from higher stages of ionization than predicted by model photospheres; so significant absorption features not coincident with the model photosphere predictions are candidates for wind lines. In regards to the latter point, we did in fact find that lines from high ionization stages were present, so we computed theoretical wind line strengths using available information about the wind and X-ray observations of ϵ CMa. The methods used for the wind predictions are based in part on those described in MacFarlane et al. (1993), and the application to ϵ CMa is explained in greater detail in § 7.

As a result of the photospheric and the wind model calculations we have two sets of lines to compare with the observed spectrum. From the TLUSTY photospheric model we use as an indicator of the line strengths the ratio, r, of the opacity at the center of a line to that in the continuum at optical depth $\frac{2}{3}$. This ratio depends on the absorbing ion as $r \propto N_l g_l f_{lu}$, where N_l is the number abundance of the lower level of the transition, which this depends on the ionization fraction of the absorber, and $g_l f_{lu}$ gives the probability of the transition. The ratio r is used instead of the predicted equivalent width because the latter is sensitive to details of the temperature structure in the outer atmosphere of the star, and as we have seen above, this is not yet well modeled for ϵ CMa. The second set of line strengths used for the identifications are from the wind model. We illustrate the predicted strengths of the lines that are expected to be present by using the ratio, τ/q_{iz}, of the wind optical depth in the line of the ionization fraction of the line producing ion. The computation of this quantity is described in § 7. Only transitions involving ground states and metastable states with lower levels having excitation energies less than 10 eV above the ground are used in the comparison.

Figures 5*a*–5*d* show the LW spectrum of ϵ CMa in $\sim$80 Å segments, from 450 to 735 Å. Plotted is the flux above the Earth's atmosphere as observed by *EUVE*. The conversion from observed count rates to fluxes uses the intrumental sensitivity and wavelength calibration as discussed in § 2. The predictions of the TLUSTY photospheric model are shown along the top of the figure. Each line from the model is identified by the ion producing the line, the line wavelength, log r, and finally an asterisk (*) is shown if the line is either a resonance line or one that originates from and excited level $\lesssim$3 eV from the ground. The lines expected to be formed in the wind are indicated along the bottom of the figure. The length of the arrow associated with each of these lines is determined by the τ/q_{iz} value for which the scale is presented on the figure.

Because of the fixed pattern noise discussed in § 2, we should not consider apparent absorption or emission features with amplitudes on the order of 10% of the continuum or less. So our focus here should be on the stronger features in the spectrum.

The most prominent photospheric feature in the LW spectrum is the He I ionization edge, which has a laboratory wavelength of 504 Å. In the data, however, this edge is displaced redward by about 6 Å. This is due to transitions to the many bound states of neutral helium with high principal quantum numbers. Some of the displacement is also due to an O III resonance line at 508 Å and to several weaker N II lines between 505 Å and 510 Å.

An especially distinctive property of the LW spectrum is the high density of spectral features. Most of these are broad, and this is both because of the moderate spectral resolution of the detector, and also because of the high density of lines that are present in the EUV range, which leads to line blending. The identifications in Figure 5 give only an indication of the degree of line blending. Nevertheless, note that most of the absorption features with depths greater than about 10% of the local apparent continuum are identified with lines or line blends predicted by the model photosphere. Our line identifications and strength predictions indicate that very few features derive even half their strength from a single ion.

Only the lines with the highest predicted strength are shown in each panel; i.e., there is a cutoff in the value of log r (which is different in each panel). Of course many weaker lines could be contributing as well. One prominent example of the effects of blends of weaker lines is the very broad absorption trough centered near 518 Å. The atmosphere model predicts numerous lines of He I, O II, Fe III, Fe IV, Si III, N II, S III, and Ar II contributing to this broad absorption. Another example is the feature near 550 Å; there are almost 50 separate Fe IV and Fe III transitions which may contribute.

The density of lines in the EUV spectrum of ϵ CMa makes continuum placement difficult, and special care will be required in studies of line equivalent widths. The large trough of blended absorption features from 515 and 560 Å seems to contain three "emission" features at 525, 545, and 560 Å, but these probably represent frequency zones with reduced line blanketing and the flux is rising toward the continuum level.

Detecting spectral evidence for a stellar wind is of great interest. It is known that the star has a stellar wind from UV observations made from the *Copernicus* and *IUE* satellites. As is common in the spectra of non supergiant B stars, the wind lines do not show a distinct shortward edge to the P Cygni absorption trough, but rather a gradual rise toward the continuum level. This means that the wind terminal speed, estimated from the "edge velocity" of the line absorption, is uncertain.

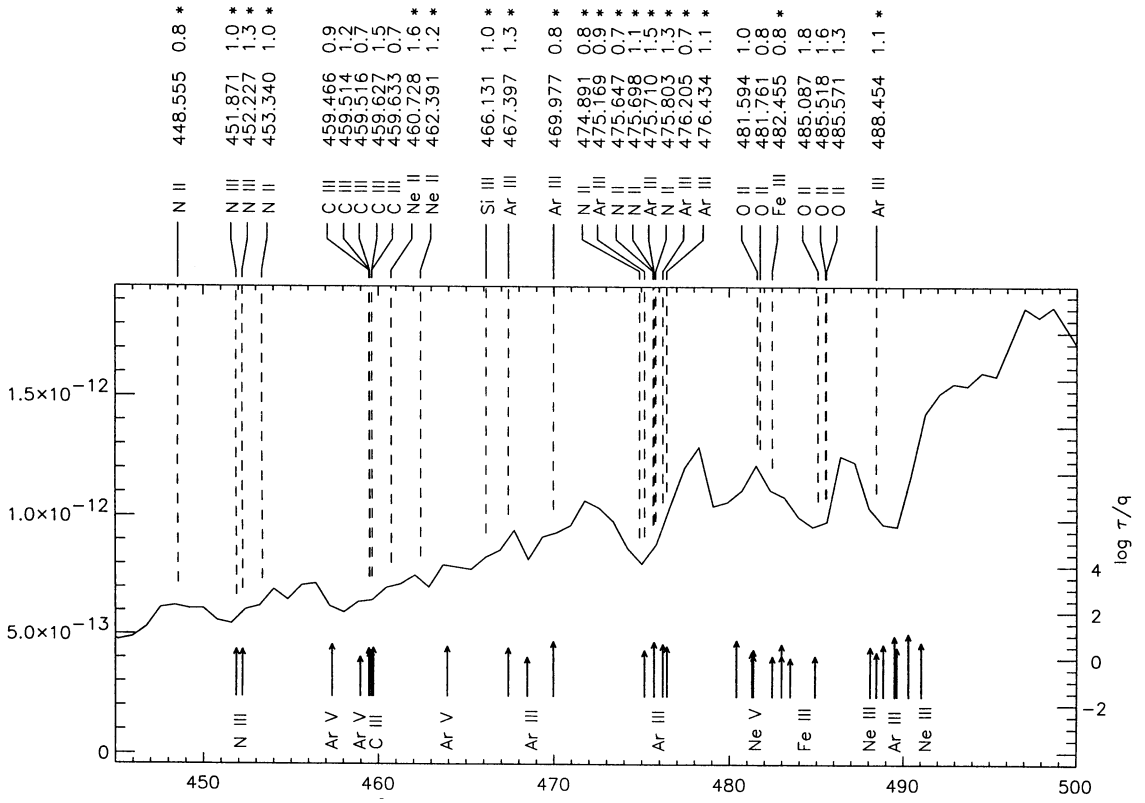

FIG. 5a

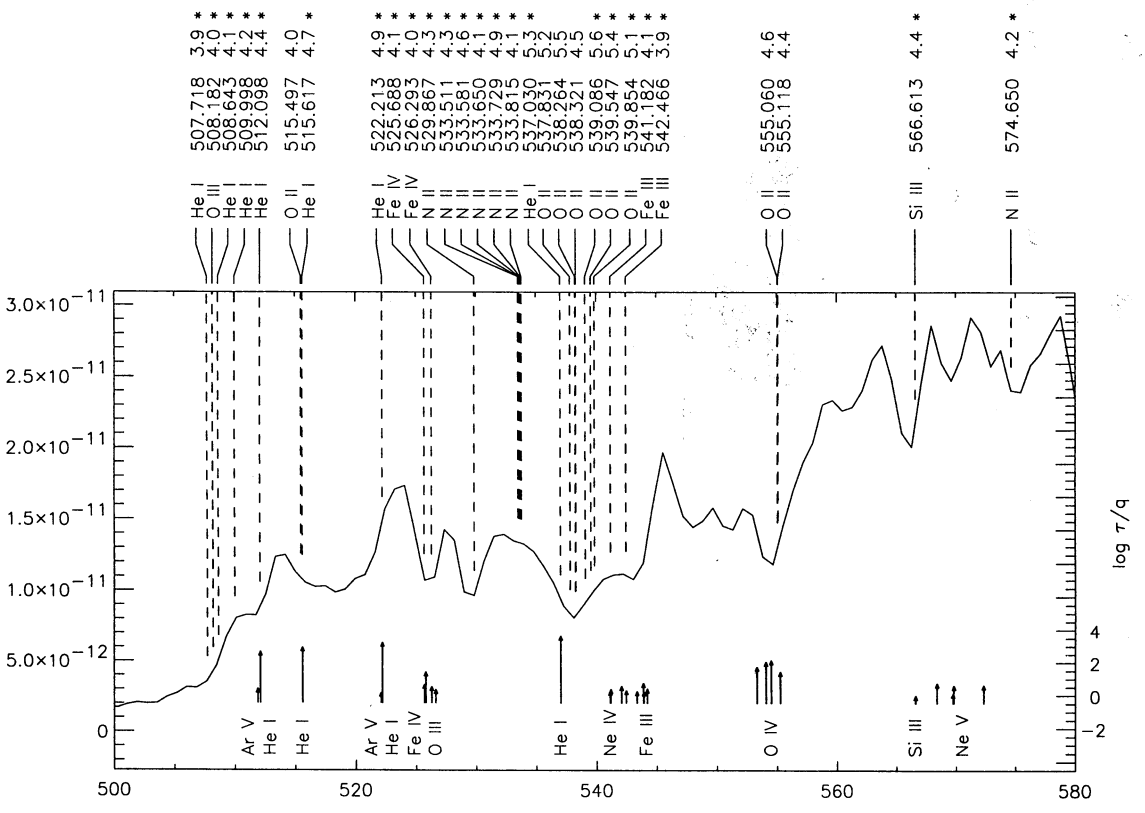

FIG. 5b

FIG. 5.—Line spectrum of ϵ CMa from 450 to 730 Å in cgs flux units at the Earth. Along the upper portion of each figure are the line identifications and indicatory line strengths in units of log r, where r is the ratio of the line center opacity to that in the continuum, which are predicted by a model atmosphere with $T_{\rm eff}$ = 21,000 K. The asterisks indicate which lines are resonance lines (lower levels with energies less than 3 eV above ground). Along the lower portions of the figure are lines that are expected to be strong in the stellar wind of ϵ CMa based on ionization calculations. The values of the wind line strength parameter can be read from the scale on the right of each panel.

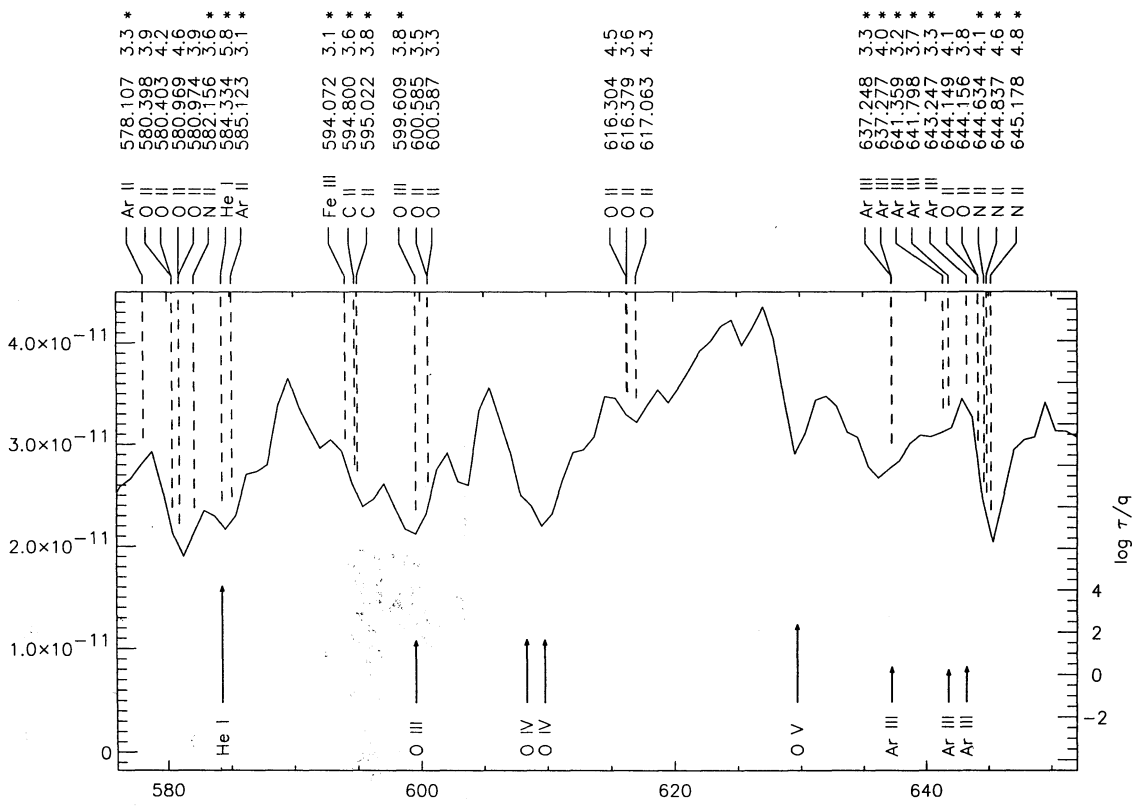

FIG. 5c

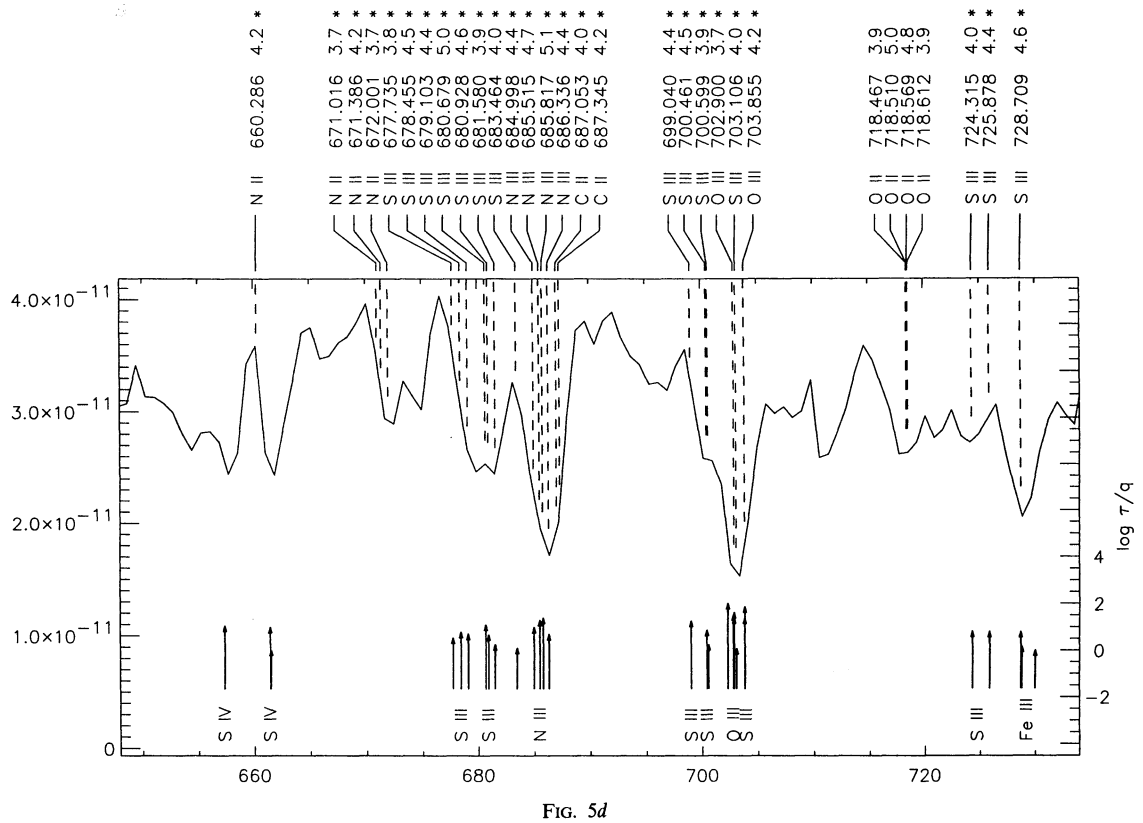

FIG. 5d

TABLE 4

WIND ABSORPTION LINES

Ion	λ (Å)	τ/q_{iz}
C III	386	35.2
N III	452	5.0
	687	58.7
O III	508	122.1
	526	25.7
	600	42.3
	703	259.1
O IV	555	328.1
	609	93.2
O V	629	239.9
Ne III	489	35.4
Ne IV	543	9.2
Ne V	569	11.2
	572	4.4
S III	678	15.0
	682	20.7
	700	27.7
	703	1.3
	725	13.1
	729	6.4
S IV	657	11.6
	661	11.1
Ar III	468	9.5
	476	15.6
Ar V	458	5.3
	460	2.9
	464	3.3
	512	2.5
	522	1.5
Fe IV	527	5.6

However the largest "edge velocity" derived from the *Copernicus* observations by Snow & Morton (1976) is 820 km s^{-1}, from the Si IV (1394, 1403 Å) resonance lines. *IUE* observations of ϵ CMa also show weak, blueshifted absorption in C IV (1548, 1551 Å) with a maximum displacement velocity of about 600 km s^{-1}, with some uncertainty introduced by blending with nearby iron lines. N V (1239, 1243 Å) also appears in the *IUE* spectrum, although its profile is less broadened. The spectral resolution of the LW spectrometer, corresponds to about 1200 km s^{-1}, which exceeds any of the estimates of the wind speed. As a result, it is not possible to distinguish between photospheric and wind lines based on the line width.

The best discriminant between wind and photospheric features in the *EUVE* data is the ionization potential of the ion producing the line. The ionization level in winds is higher than in the photosphere as a result of the X-rays that are present in the wind, and ϵ CMa is detected at X-ray energies. We identified several strong lines from high-ionization stages, such as the feature at 629 Å at the location of a strong O V resonance line. This is an ionization stage which is at a much higher level than is expected in the photosphere. Other candidates for the wind lines are identified in Figure 5, and listed in Table 4. In some cases such as O III (at 703 Å), there may well be contributions from both the photosphere and wind. § 7 contains a discussion of the production of enhanced ionization stages that result from the X-ray photoionization.

It appears that the wind lines contribute significantly to the absorption observed by the LW spectrometer. The case of oxygen is especially interesting because the LW spectrum shows a wide range of ionization stages, in the strong resonance line feature from O II (430 and 538 Å), O III (508 and 703 Å, with metastable lines near 526 and 600 Å), O IV (555 and 609 Å), and O V (629 Å). As is indicated in the figure there may be some photospheric absorption from other elements contributing to some of these features. Note that the wind optical depths can be quite large for the oxygen lines, reaching $\tau \sim 10^2$ for the dominant ionization stages. Oxygen ions with $q_{iz} \gtrsim 10^{-2}$ in the wind are capable of producing significant absorption, and one would expect that such an abundance would exist at more than one of the oxygen ionization stages.

Finally it is interesting to note that there are several features in the LW spectrum for which neither the atmosphere nor the wind models can account. These include the features at 479, 604, 695, and 711 Å. In several cases there are photospheric lines which are expected to be weakly present, but they are far below the observed strengths at these wavelengths.

In summary: the strong lines predicted by the atmosphere model to be present are in fact seen. A major property of the EUV line spectrum of ϵ CMa is the high degree of line blanketing. This can have significant effects on the temperature distribution in the atmosphere of the star. Several of the wind features which are expected to be strong based on our wind ionization model are clearly present, and these provide additional diagnostics for studying the wind properties.

6. EMISSION LINES

There are several emission lines detected shortward of 380 Å. In this section we identify them and derive their fluxes, and where possible, their widths. In the next section we interpret the lines in terms of a stellar wind with both a hot and a cool component.

Several of these emission lines are from low-ionization stages of oxygen and helium. Two of these represent the strongest emission features we see in the spectrum of ϵ CMa (see Table

TABLE 5

LOW ION EMISSION LINES

Wavelength (Å)	Spectrometer	Ion	Counts	Flux[a] (ergs cm^{-2} s^{-1})	Luminosity[b] (ergs s^{-1})
374	LW	O III	286 ± 24	$(3.39 \pm 0.28) \times 10^{-13}$	3.6×10^{30}
304	LW	He II	1571 ± 55	$(3.21 \pm 0.11) \times 10^{-12}$	2.4×10^{31}
304	MW	He II	988 ± 45	$(2.53 \pm 0.12) \times 10^{-12}$	2.0×10^{31}
256[c]	MW	He II	<40	$<1.5 \times 10^{-13}$	$<9.2 \times 10^{29}$
243	MW	He II	<11[d]	$<4.1 \times 10^{-14}$	$<2.4 \times 10^{29}$

[a] Observed flux at the Earth.

[b] Assuming a distance of 188 pc and corrected for interstellar attenuation with $N_{H^0} = 1 \times 10^{18}$, $N_{He^0} = 1 \times 10^{17}$.

[c] Blended with Si X and S XIII.

[d] 1 σ upper limit.

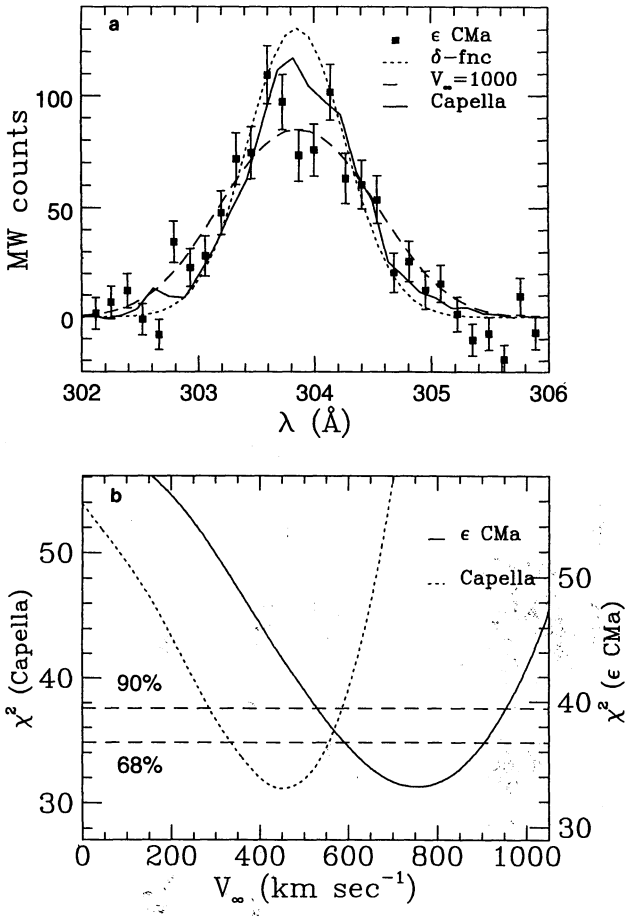

FIG. 6.—(*a*) He II Lyman-α lines of ϵ CMa and Capella, along with delta function and 1000 km s^{-1} models. (*b*) The run of χ^2 with line width for ϵ CMa and Capella. A parabolic line profile was assumed. The 68% and 90% confidence limits for a joint probability distribution with three degrees of freedom are shown (Lampton et al. 1976).

5). The single strongest emission line in our data is the He II Lyman α line at 303.8 Å. It appears in both the LW and MW spectra. In our discussions we will refer to the MW detection of this line, since the spectral resolutions is superior to that of the LW spectrometer and the line is closer to the center of the MW bandpass. In Figure 6 we show this line along with the same feature as it is seen in the *EUVE* observation of Capella (Dupree et al. 1993). We also plot in this figure a delta function and an optically thick wind line profile using a terminal velocity of 1000 km s^{-1} for comparison. Both models have been folded through the detector response matrix.

To determine the width of the line, we performed χ^2 minimization with models in which line width, position, and amplitude were free parameters. We used several different intrinsic line shape functions: box, Gaussian, and the parabolic shape expected for a wind with monotonically increasing velocity. Because the width of the feature is dominated by the instrumental broadening, the choice of line shape proved to be relatively unimportant. We derive a velocity of $v_\infty = 750 \pm 150$ km s^{-1} using the parabolic line profile given by $F \propto [1 - (\Delta v/\Delta v_{max})^2]$, where $\Delta v_{max} = v_\infty v/c$. We compare the profile with that of Capella, which we expect to be intrinsically narrow. For Capella we find 425 ± 50 km s^{-1}. The values of χ^2 as a function of line width, along with confidence limits, are shown in Figure 6 for both ϵ CMa and Capella. Even if the spectral resolution has been underestimated in the most recent calibration, we can see that the feature in ϵ CMa must be velocity broadened by at least a few hundred km s^{-1} relative to the same feature in the spectrum of Capella.

We also see a broad feature near 256.3 Å, which is the lab wavelength of the He II Lyman-β line; this feature is shown in Figure 7. The breadth of the feature is probably due to blending with lines of Si X and S XIII. Due to this blending, it is impossible to accurately determine the flux in the helium Lyman β line. However, if we assume that the intrinsic width of this line cannot be more than 1000 km s^{-1}, then we can place an upper limit on the He II Lyman β flux of 40 counts. The Lyman-γ line at 243 Å is a nondetection with a 1 σ upper limit of 11 counts.

The second strongest emission line seen in the spectrum, with over 200 counts, is centered on 374 Å and is identified as O III. This is a resonance line transition whose upper level may be populated subsequent to pumping of O III by He II Lyman α; the first step by the Bowen fluorescence mechanism, as will be discussed later. We analyzed the width of the 374 Å line in the same manner as described above for the 304 Å line. The velocity associated with the width was not well constrained because of the uncertain relative strengths of the components of the multiplet, but the derived width was at least consistent with that derived for the 304 Å line.

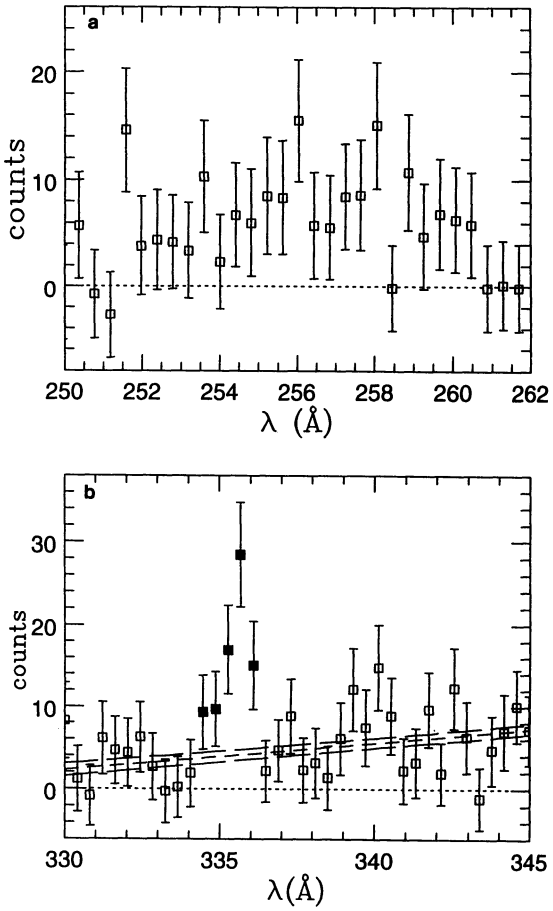

FIG. 7.—Two of the emission lines detected in the MW spectrometer: (*a*) Blend of lines centered on the He II Lyman-β feature at 256 Å and (*b*) Fe XVI at 335 Å, shown with the continuum fit.

TABLE 6

HIGHLY IONIZED IRON EMISSION LINES

Wavelength (Å)	Spectrometer	Ion	Significance[a]	Counts	Flux (ergs cm^{-2} s^{-1})	log $T_{\epsilon_{max}}$[b] (K)
171	SW	Fe IX	0.96	29 ± 9	1.95×10^{-13}	5.90
181	MW	Fe XI	0.94	29 ± 10	1.12×10^{-13}	6.09
284	MW	Fe XV	0.99	34 ± 10	1.56×10^{-13}	6.32
335	MW	Fe XVI	>0.99	60 ± 12	2.38×10^{-13}	6.45

[a] Confidence level at which the null hypothesis can be rejected; i.e., the probability that the χ^2 for the model (zero flux) should be less than the observed value.

[b] Temperature of peak emissivity in the Raymond–Smith equilibrium model.

We also report tentative identifications of four emission lines which arise in hot plasmas ($T \sim 10^6$ K). These lines, which are all due to iron, are listed in Table 6. We determined the significance of each line by testing againt the null hypothesis. The confidence level quoted is that for rejecting the null hypothesis. Formally it is the likelihood that zero intrinsic flux would give a χ^2 lower than the observed value. The fluxes were determined by summing the counts over a range of bins corresponding to the expected line width. We assume that the plasma can be described by a collisional ionization equilibrium model (as will be discussed in § 7). In this case the emissivity of each line is a relatively sharp peaked function of temperature. We list the temperature of peak emissivity of each line in the Raymond–Smith model in Table 6.

These four emission lines are weakly detected, with only the Fe XVI line at 335 Å exceeding the 4 σ significance level, and it is shown in Figure 7. However, each of the four lines is expected to be very strong in equilibrium models described by temperatures between 0.5 and 3 million degrees. More confident identifications and better flux determinations will be possible when more observations of ϵ CMa are obtained during the second cycle of guest observations.

7. INTERPRETATION OF THE EMISSION LINES

We have seen in § 5 that the LW absorption line spectrum can be explained as arising in the photosphere and in the wind. The emission lines, however, require additional interpretation. This is because the strengths of the high-ionization emission lines are less than we had expected based on the *ROSAT* observations, and the emission lines of He II at 304 Å and O III at 374 Å were unexpected based on equilibrium models. In this section we analyze the lines from both the high and low stages of ionization, and then attempt to determine if there is a physical connection between the two. We shall incorporate in our discussion the knowledge that ϵ CMa is an X-ray emitter for which some information is available regarding the source temperatures and emission measures. The X-rays from early-type stars are generally thought to originate in shocks distributed in the winds and we will make use of that picture here.

7.1. *High-ionization Emission Lines*

Emission lines of highly ionized metals were expected to be present in the SW and MW spectrometers, based upon models of similar B stars by MacFarlane et al. (1991) and the *ROSAT* detection of ϵ CMa. The *ROSAT* spectrum of ϵ CMa is rather soft, with a majority of counts below the carbon edge at 0.28 keV, or above 45 Å. *ROSAT* sensitivity extends up to 128 Å, so these two satellites probe an overlapping wavelength range. The X-ray spectrum is adequately fit with a two-temperature Raymond–Smith emission model with temperatures of 2 and 8.5 million degrees, or alternatively temperatures of 1 and 5.5 million degrees (Drew et al. 1994). The derived *ROSAT* model parameters (either set) imply that we should see strong emission, with several lines each having well over 100 counts in our exposure. However, the fluxes we observe in the emission lines are many times lower than this. Additionally, neither of the *ROSAT* two-temperature models predict the combinations of lines which are observed.

There are two possibilities that might explain the difference between the observed line strengths and those compatible with the published *ROSAT* soft X-ray fits. Models with just two source temperatures might overestimate the power in those emission lines that are predominant at the two temperatures, relative to models having a distribution in temperatures. Second, there could be somewhat higher wind and ISM attenuation of photons at EUV wavelengths to which the harder energy response of the *ROSAT* PSPC is relatively insensitive. This is plausible given the photoionization opacity peaks near threshold, and the He^+ threshold (as well as many L-shell thresholds) lies in the EUV.

In the Raymond–Smith ionization equilibrium models used to predict line emission strengths, the four iron lines that we observe in the EUV have their maximal contribution at different temperatures, ranging from log $T = 5.9$ to 6.45. In order to fit the data we must consider models with a range of temperatures. A model with a *continuous* distribution of temperatures might alleviate the line flux discrepancy, since the radiated power will be spread out among more lines, and so no single line would be expected to have the high count rates that are predicted by one- or two-temperature models. Indeed, hydrodynamical simulations suggest that there will be a wide distribution of temperatures in the stellar wind. For example, Cooper (1994) finds that the emission measures of the shocks in winds tend to follow a power law distribution versus temperature of the form $EM = EM_0\, T^{-\alpha}$. We therefore produced Raymond–Smith models with such a temperature distribution, and fit these models both to the *ROSAT* data and to the iron emission lines seen with *EUVE*. The *ROSAT* data alone were well fit by models with slopes between -0.4 and -1.0 in the temperature interval $5.7 \lesssim \log T \lesssim 6.8$, and with overall emission measures of about 5×10^{53} cm^{-3}. Although the power-law emission measure model does not lead to significant differences in the *ROSAT* fits, it has a clear advantage when the *EUVE* data on emission line strengths are considered. The power-law emission measure distribution model predicts emission lines that are weaker and closer to the observed line strengths, than the two-temperature model. It also reproduces all four of the lines we detect. But, despite the improvement, the observed lines were still 2 to 3 times weaker than these models predicted.

This suggests that additional absorption by ionized material should be included in our spectral models. By including a column density equivalent to a cosmically abundant gas with $N_H = 1 \times 10^{20}$, but with all of the hydrogen ionized and with 90% of the helium doubly ionized, we are able to achieve good agreement between the *EUVE* and *ROSAT* data sets. With this level of ionization of helium, metals make a significant contribution to the opacity in the EUV spectral range. The acceptable models have emission measures of 7×10^{53} cm^{-3} and slopes steeper than -1 in the range $5.6 \lesssim \log T \lesssim 6.9$. Most of the additional absorption could be in the stellar wind and still be consistent with a mass loss rate of order $10^{-8}\ M_\odot$ yr^{-1}. But because of the uncertain level of ionization in the ISM, some fraction of this additional absorption by ionized material may arise there. A more detailed analysis will be required to estimate the ISM and wind contributions to the attenuation, or to find a better estimate of the wind mass-loss rate. Nevertheless, our initial study has indicated that the *ROSAT* and *EUVE* observations can be reconciled if they are modeled in terms of a spread in emission temperature that is consistent with current shock models, and a plausible level of attenuation at EUV energies. We note the importance of the *EUVE* observations in narrowing the acceptable model parameter space which was originally defined by *ROSAT*.

7.2. *Helium Emission Lines*

Lyman-α and Lyman-β emission lines of He II are observed in the *EUVE* spectrum. Here we use the fluxes in these lines to study where these emission lines are formed. Firstly, we note that these lines could not be formed in the outer layers of the photosphere. There is simply too little hard radiation in a 21,000 K star, to produce a significant abundance of the $n = 2$ level of He^+, or of He^{++}, which would then produce the Lyman-α line after recombining. Also the temperature in the outer layers of the photosphere is too cool to lead to the collisional production of the Lyman-α line. Our detailed LTE and non-LTE model calculations confirm these conclusions. Additionally, the Lyman-α line is broadened by at least several hundred km s^{-1}, so the wind must be considered the source of the line.

Here we first derive the ionization abundance that is needed to form a strong line and then determine whether the X-rays, known to be present in the wind, are able to produce the required ionization abundance. Since the analysis also provides information regarding neutral helium, this species is also considered briefly.

The helium lines observed in the *EUVE* spectrum can be affected by the wind both because of the high fractional abundance of helium and because the observed He I absorption lines and He II emission lines are all resonance lines. The optical depth of a wind line can be written as (see, e.g., Castor & Lamers 1979):

$$\tau(r) = \left(\frac{\pi e^2}{mc}\right) f_{ul}\, \lambda_0\, A_E \left(\frac{dv}{dr}\right)^{-1} n_w(r) q_{iz}(r) \left\{ f_l(r) - \frac{g_l}{g_u} f_u(r) \right\} \quad (1)$$

$$= (1.68 \times 10^4)(f_{ul}\, \lambda_0\, A_E) q_{iz}(r) f_l(r) \left(\frac{\dot{M}}{10^{-8}\ M_\odot\ \mathrm{yr}^{-1}}\right) \times \left(\frac{R_*}{R_\odot}\right)^{-1} \left(\frac{v_\infty}{1000\ \mathrm{km\ s}^{-1}}\right)^{-2}, \quad (2)$$

where the spatial-dependent quantities are the ionization fraction, $q_{iz}(r)$, and the fractional populations of the lower and upper energy levels, $f_l(r)$ and $f_u(r)$ and f_{ul} is the oscillator strength, λ_0 is the wavelength in Å, A_E is the fractional abundance (assumed $=0.078$ for He), R_* is the stellar radius, $\dot{M}$ is the mass-loss rate, and v_∞ is the maximum wind velocity. The convenient form shown in equation (2) was derived assuming the velocity law of $v(r) = v_\infty(1 - R_*/r)^{1/2}$. Using $\dot{M} = 8 \times 10^{-9}\ M_\odot\ \mathrm{yr}^{-1}$, $v_\infty = 800$ km s^{-1}, and $R_* = 16.2\ R_\odot$, the optical depth for the strongest He I and He II lines are

$$\tau(r) = \begin{cases} 1.6 \times 10^4 q_{\mathrm{He\ I}}(r)\,, & (\mathrm{He\ I}: \lambda = 584\ \text{Å})\,, \\ 1.3 \times 10^4 q_{\mathrm{He\ II}}(r)\,, & (\mathrm{He\ II}: \lambda = 304\ \text{Å})\,, \end{cases} \quad (3)$$

where we have assumed $f_l(r) \approx 1$ (i.e., each ion is predominantly in its ground state). Thus, unless He is fully ionized in the wind of ϵ CMa, the He I and/or He II lines should be affected by the wind. A similar analysis holds for the resonance line of higher-Z species identified in Figure 5, although the chemical abundances are lower by two orders of magnitude or more.

Let us now consider the origin of the He II emission in the wind. Since we know from the X-ray observations that there is hot material in the wind, we first consider the possibility that the He II emission lines arise directly from the hot X-ray producing material. This could occur, for example, in a situation where a hot, shock-heated plasma region is *external* to the cool, lower velocity region of the wind (Abbott & Friend 1989; Drew et al. 1994). In such a situation, the He II lines might not be subject to outer wind attenuation effects if the temperature there were high enough to sufficiently reduce the He II ionization fraction. This external line formation region explanation can be rejected by examining the He 304 Å and 256 Å fluxes predicted for high-temperature plasmas. Figure 8*a* compares the observed fluxes (*horizontal lines*) with those calculated using the formula:

$$F_L = \frac{EM_X\, \Lambda_L(T)}{4\pi D^2}\,, \quad (4)$$

where the X-ray emission measure, EM_X, was taken to be the *ROSAT* value of 7.2×10^{53} cm^{-3}, D is the distance to ϵ CMa, and $\Lambda_L(T)$ was computed using the XSPEC code (Raymond & Smith 1977). Figure 8*a* clearly shows that the 304 Å flux (*solid curve*) is lower than the observed value for temperatures above 2×10^5 K. The measured upper limit to the 256 Å flux can be used as an additional constraint. Figure 8*b* shows the calculated ratio of the 304–256 Å flux is lower than the observed lower limit, for $T \geq 10^5$ K. Note also that as the temperature decreases to 2×10^5 K, the He II ionization fraction rises to 0.02, which means that the He II lines again become optically thick (see eq. [3]). We therefore conclude that the He II emission lines are optically thick, and they originate from "cool" regions of the wind where $10^4\ \mathrm{K} \leq T \leq 10^5$ K.

To predict the He ionization distribution in the "cool" wind of ϵ CMa, we have performed wind ionization balance calculations using the models discussed by MacFarlane et al. (1993). In these calculations we assumed a spherically expanding, isothermal wind ($T_{\mathrm{wind}} = T_{\mathrm{eff}}$) with $v(r) = v_\infty[0.01 + 0.99(1 - R_*/r)^{0.8}]$. The values of v_∞ and R_* were those given for equation (3). Atomic level populations for H and He were calculated at each point in the wind by solving multilevel statistical equilibrium equations self-consistently with the radiation field. A total of 19 atomic levels were considered for H and He, with levels up to $n = 6$ for H I and He II. The photospheric continuum radiation field used in the model was based upon UV and EUV observations. X-ray radiation was

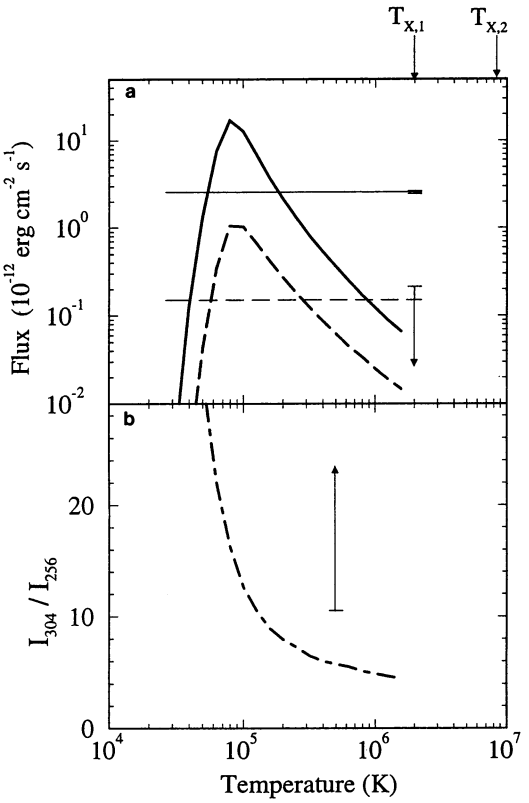

FIG. 8.—Panel (*a*) compares the observed flux of the 304 Å line (*solid horizontal line*) and the flux of the 256 Å line (*dashed horizontal line*) vs. model calculations of the line strengths, which are functions of the assumed wind temperature. The two temperatures associated with the *ROSAT* fit to the X-ray emission are indicated by the symbols at the top of the figure. Panel (*b*) shows the calculated ratio of the 304–256 Å lines vs. temperature. The observational lower limit on this ratio is indicated by the arrow.

included, using the parameters from the two-temperature fit of Drew et al. (1994) to *ROSAT* observations: $T_{X,1} = 2 \times 10^6$ K, $EM_{X,1} = 5.3 \times 10^{53}$ cm^{-3}, $T_{X,2} = 8.4 \times 10^6$ K, and $EM_{X,2} = 1.9 \times 10^{53}$ cm^{-3}. The peak emission was assumed to occur at $r \simeq 1.3\ R_*$ ($x_0 = 1.3$ and $\alpha = -3$ in eq. [10] of MacFarlane et al. 1993). The radiation field at each point in the wind was computed using a multiangle impact parameter model (see Mihalas et al. 1975).

Results for the He ionization distribution are shown in Figure 9, for two cases: one assuming a radially distributed source of X-ray emission (shock model), the other in which X-rays were neglected. In each case, the mass-loss rate was taken to be $1.6 \times 10^{-8}\ M_\odot$ yr^{-1}. This value was selected because it produced a He II 304 Å line intensity in the shock model calculations consistent with the observed value. Without the inclusion of X-rays, the line intensity was about a factor of 25 too low. The dashed curves represent results from the calculation with no X-rays included. In this case, it is seen that He^+ is the dominant ionization stage throughout the wind, while He^0 and He^{++} are trace species with ionization fractions less than 10^{-3}. Results from the distributed X-ray source calculation are indicated by the solid curve. He^{++} exceeds the He^+ fraction throughout the higher speed portion of the wind ($r \geq 1.3\ R_*$). The He^+ fraction is approximately unity near the base of the wind where the density is high and recombination becomes more effective. It is clear from these results that the X-ray–emitting plasma, which is observed by *EUVE* in the form of Fe emission lines, plays a central role in establishing the He ionization balance in the wind. This result raises the possibility that the X-rays may significantly raise the temperature of the wind since the bound-free heating/cooling rates are of similar form to the photoionization/recombination rates.

Figure 9 also shows that for He I the fraction is quite small, with $q_{\rm He\,I} \lesssim 2 \times 10^{-5}$ for wind velocities $\gtrsim 0.1 v_\infty$. This suggests that wind absorption of the He I lines longward of 504 Å should be minimal, with $\tau \sim 10^{-1}$ for the 584 Å line (see eq. [2]). On the other hand, all of the He II resonance lines from 304 Å to the 228 Å edge should be optically thick, with τ ranging up to $\sim 10^4$. We therefore conclude that the formation of the He I absorption lines is largely photospheric, while the He II emission lines are strongly influenced by the wind properties.

Figure 10*a* shows the location in the wind where the 304 Å line emission originates in our ionization calculations that include X-rays from shocks. The luminosity in the line was calculated as (Klein & Castor 1978):

$$L(r) = 4\pi\, \Delta E_{ul}\, A_{ul} \int_{R_*}^{r} n_u(r')\{\beta(r') - \beta_c(r')\} r'^2\, dr' , \qquad (5)$$

where ΔE_{ul} and A_{ul} are the transition energy and spontaneous emission rate, respectively, $n_u(r)$ is the number density in the upper level, $\beta(r)$ is the local escape probability, and $\beta_c(r)$ is the probability the photon is occulted by (lost to) the star. The solid curve in Figure 10*a* represents the spatial dependence of the scaled emissivity, and indicates the source region for the emergent line photons. The dashed curve represents the cumulative luminosity integrated outward from the stellar photosphere. The peak emission occurs at a velocity of $0.3 v_\infty = 240$ km s^{-1} (or $r \approx 1.3\ R_*$), which is simply an artifact of the dis-

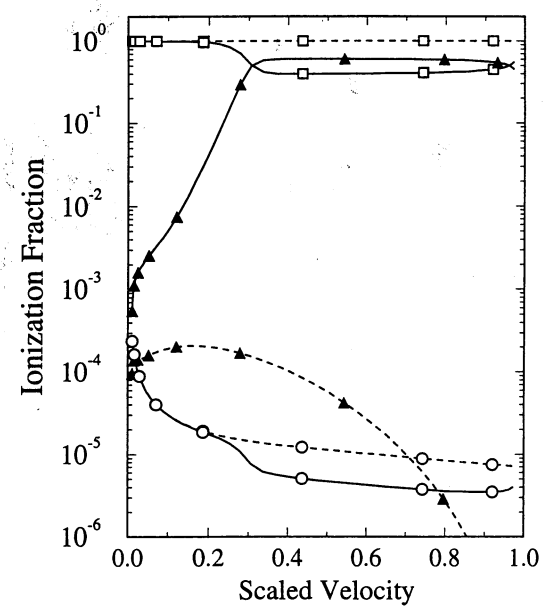

FIG. 9.—Ionization fractions of the three stages of helium vs. location in the wind as identified by the scaled velocity [$v(r)/v_\infty$]. Results are shown for two cases; one in which there is no ionization caused by X-rays in the wind (*dashed lines*), and the other in which there are X-rays from shocks in the wind (*solid lines*). In the latter case the X-ray flux emergent from the wind is consistent with the X-ray flux observed by the *ROSAT* satellite. The circles represent He^0, the squares He^+, and the triangles He^{++}.

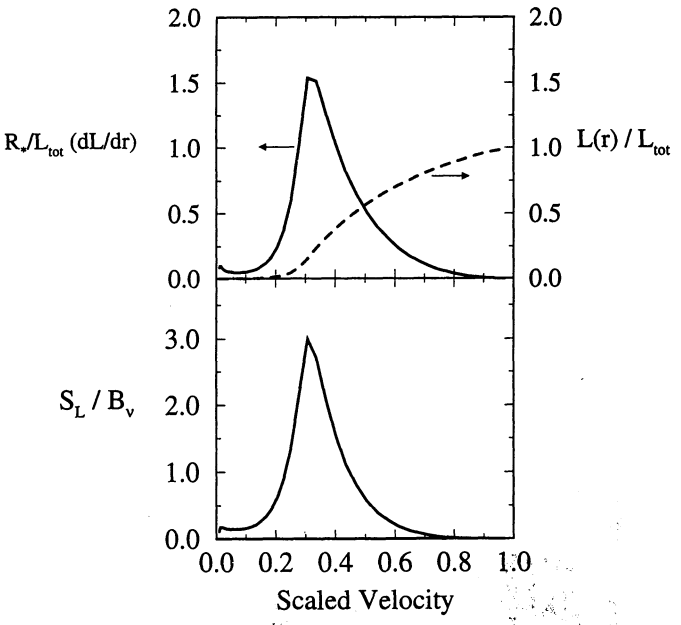

FIG. 10.—(*a*) In the upper panel the solid line shows the contribution to the 304 Å line as a function of the velocity in the wind, based on the shock model which produced the ionization distribution of the previous figure. The peak occurs where it does because that is roughly the location of the maximum contribution to the X-ray emission used in the calculation. The dashed line indicates the growth of the contribution to the full line luminosity that is observed. (*b*) Curve in the lower panel shows the radial dependence of the line source function scaled to the Planck function in the wind of ϵ CMa.

tributed X-ray source peaking at this location. This is just one model that produces agreement with observations of the X-ray spectrum and the He II line emission, and should not be considered unique. Nevertheless, our results do show that the He 304 Å line flux can readily be produced in the cool portion of the wind.

The radial dependence of the line source function, scaled to the Planck function with $T = 21{,}000$ K, it is shown in Figure 10*b*. This is also seen to peak where the X-ray emission is strongest in the calculation. Note that the source function exceeds the Planck function in this region. This occurs because the $n = 2$ level of He^+ is populated by recombination of He^{++}, which in turn is being populated to an anomalously high degree by X-ray–induced photoionization. This strong source of emission at 304 Å leads to pumping of the very coincident O III resonance lines.

In summary, we find that the He II emission lines are most likely formed in the portions of the wind that are "cool" and the emission results because of the X-ray photoionization of the wind. The analyses in this section show that there is an interesting interplay between the line emission observed shortward of 400 Å. The X-rays (traced by the Fe IX to Fe XVI lines) influence the He II ionization distribution, which in turn, via the He II 304 Å line and the Bowen mechanism, excites the O III 374 Å line.

7.3. *The Bowen Fluoresence Lines*

Figure 11 shows the He II Lyman α line and the O III resonance lines at 374 Å. Note that for the helium line at 304 Å there are a number of O III resonance lines that overlap in wavelength. Cascade from the excited levels of O^{++} leads to near-UV lines such as 3444 Å and 3341 Å which are particularly prominent in planetary nebulae (Bowen 1935), Seyfert galaxies and QSOs (Eastman & MacAlpine 1985), and in X-ray binaries (Deguchi 1985). The final step in the cascade leads to a EUV resonance multiplet near 374 Å, which is seen to be strongly in emission in ϵ CMa (see Fig. 11). This *EUVE* observation is the first to show evidence for the Bowen fluorescence process in an atmosphere of an early type star.

There is a second stage to the Bowen mechanism, which again we can illustrate from Figure 11. Note that the O III 374 Å line coincides with resonance lines of N III. The cascade from the excited levels of N III leads to optical lines near 4640 and 4100 Å (Kallman & McCray 1980). The final step in the N III cascade leads to emission at 452 Å. Referring back to Figure 5*a*, we see that the 452 Å line is not in emission. The reason for this can be seen by noting the flux levels at 374 and 452 Å. After correcting for a ISM column density of 1×10^{18} cm^{-2} the flux at the peak of the O III 374 Å line, which pumps the N III resonance, is 6×10^{-13} while the continuum flux at 452 Å is 3×10^{-12}; or a factor of about 5 higher. The increase of the continuum flux is just too rapid between 374 and 452 Å, for a weak line to be seen at the latter wavelength. For similar reasons we should not expect to see the optical lines associated with the Bowen fluorescence mechanism, nor an optical recombination line of He II at 4686 Å. It is a fortunate circumstance that we see even the two ground state transitions of the Bowen Mechanism at 304 and 374 Å. For if the star were hotter, the lines would likely not be observable above the continuum; if the star were cooler, the wind and X-ray emission would be too weak to form the lines so strongly in emission.

The luminosity of the He II 304 Å line is 2.0 or 2.4×10^{31} ergs s^{-1} (MW and LW respectively) and that for O III 374 Å is about 3.6×10^{30} ergs s^{-1}, after accounting for the interstellar attenuation at the two wavelengths. This gives a ratio of these two lines of between 5 and 7. If both lines were optically thin and formed by recombination the ratio would be much higher than this because of the higher abundance of helium. The ratio is relatively low because of the large optical depth in the He II Lyman-α line. It is the scattering of the line photons and the occasional conversion to O^{++} excitation that gives rise to the Bowen fluorescence mechanism. Although we have not yet carried out detailed wind models that include the effects of the Bowen fluorescence, it is possible to come to some conclusions based on existing nebular models. Kallman & McCray (1980) provide branching ratios for cascades within the O^{++} ion, as well as figures for calculating the Bowen line yields. All of the cascades leading to the 3444 Å line for example must be followed by the 374 Å line that we observe. To get the observed 304/374 Å line ratio of roughly 6, requires an optical depth in the helium Lyman α line of about 10^4 using the Kallman and McCray analysis. This is quite similar to the value quoted in equation (3) and in the subsequent discussion. So the 374 Å line strength in ϵ CMa is consistent with that expected from the Bowen fluorescence mechanism.

The model calculations to find the emission in the He II 304 Å line (see § 7.2) also included line transitions in the O^{++} ion. When accounting for all recombination, cascade and collisional and radiative excitations, *other* than the Bowen fluorescence, the calculations consistently yielded 374 Å fluxes which were a factor of 3 or more lower than those observed. The pumping of the upper level of O^{++} by He II 304 Å seems to be necessary to reproduce the observed 374 Å emission.

This is the first time that the ground state transitions involved in the Bowen mechanism have been observed in a star other than the Sun. The mechanism has been well studied in

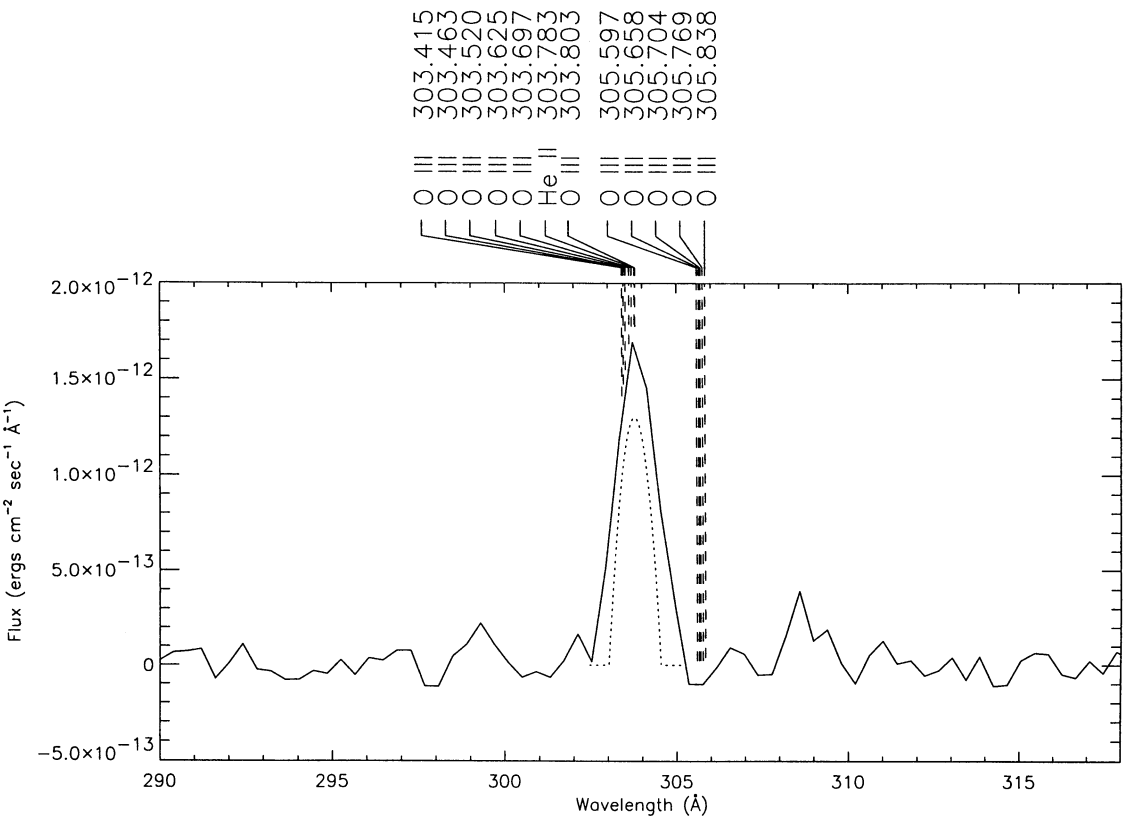

FIG. 11*a*

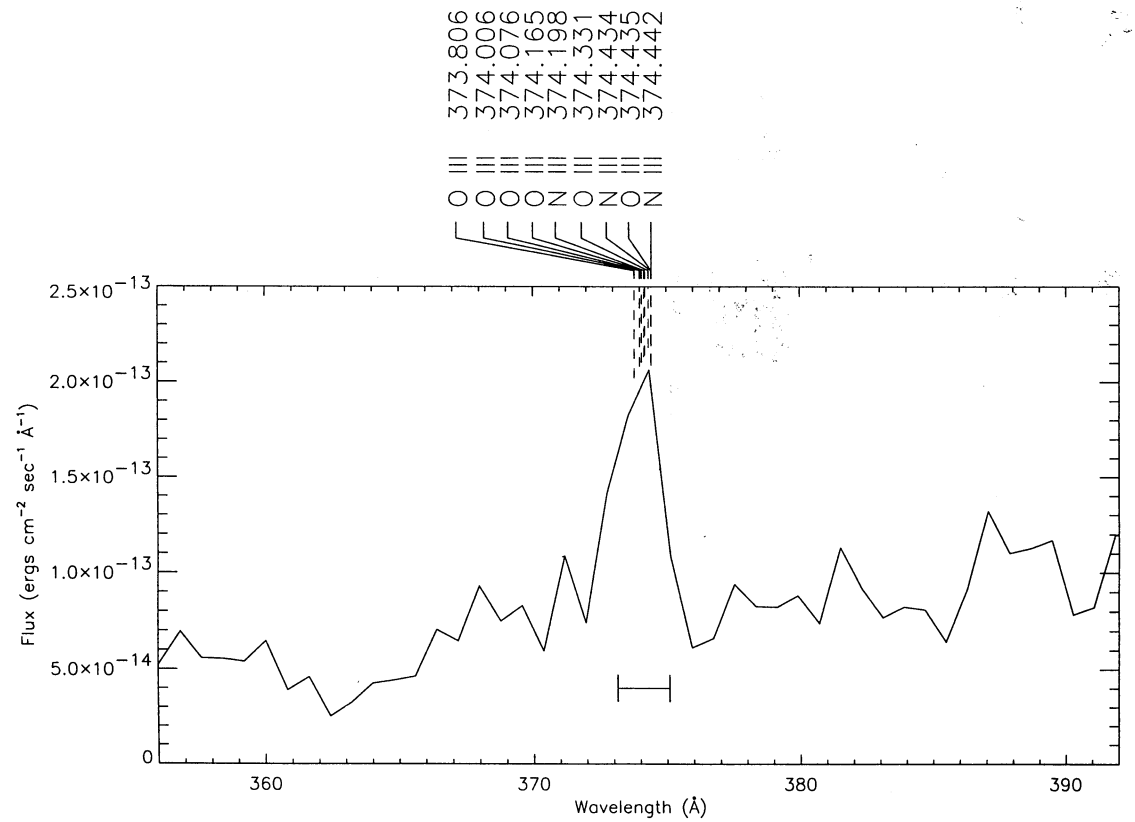

FIG. 11*b*

FIG. 11.—Emission lines (*a*) predominantly from He II at 304 Å and (*b*) from O III at 374 Å that play prominent roles in the Bowen fluorescence mechanism. Note the overlap of these two features with resonance lines of other ions. In (*a*) the intrinsic line shape (as determined in § 6) is indicated by the dotted line. In (*b*) a rough indication of the intrinsic line width is indicated by the bar. The extremes of the bar indicate the FWHM of the bluest and reddest components of the O III multiplet, assuming a parabolic line shape and $v_\infty = 750$ km s^{-1}.

other areas of astronomy, and now it should prove to be useful for understanding radiation processes operating in stellar winds.

8. SUMMARY

This paper reports on the first pointed *EUVE* observation of an early-type star, which was observed for an effective time of about 60,000 seconds.

The B2 II star ϵ CMa is the brightest object in the EUV sky. In part, this is because it lies in a rarified tunnel in the interstellar medium, so even though it is at a distance of 188 pc the attenuation of the EUV light by interstellar matter is very small. Because of its large EUV flux, ϵ CMa is the dominant source of ionization of the interstellar gas within a few parsecs of the Sun. The emergent flux from ϵ CMa in the hydrogen Lyman continuum exceeds the value expected from model atmospheres by a factor of about 30, even when the effects of line blanketing are accounted for. Two possible causes of this large flux were considered: non-LTE effects and an unexpectedly high temperature in the outer atmosphere. We concluded in favor of the latter explanation because the region of the atmosphere where the Lyman continuum forms coincides with that for the IR free-free continuum at 12 and 25 μm. The star shows an infrared excess at these two wavelength regions, and since free-free emission is an LTE process, the excess must be due to a temperature enhancement in the outer atmosphere. The star also shows a surprisingly large flux in the He^+ continuum shortward of 504 Å. LTE models which include line blanketing predict a flux that is several orders of magnitude lower than what is observed, while the TLUSTY model underestimated the flux by about the same factor that it underestimated the H Lyman continuum flux. These disagreements with the best available model atmospheres pose real problems for stellar atmospheres theory. It appears that other effects might need to be accounted for, and backwarming by the shocked wind is one of the possibilities that will be explored in the future.

The *EUVE* LW spectrometer has provided a rich absorption line spectrum. We used a comparison non-LTE model to make identifications of many of the lines, many of which were blends within the spectral resolution of the instrument. We detect all of the strong resonance lines which were predicted by the atmosphere model. We also identify some photospheric features which are blends of many nonresonance lines. Several features were explained as arising from resonance lines that should be strong in a stellar wind. Some of these lines were from somewhat higher ionization stages than are present in the photosphere, and these stages can be caused by the effects of the stellar X-rays and Auger ionization.

Further information concerning the outer atmosphere of ϵ CMa was provided by the short and medium wavelength spectrometers. Four lines of high ionization stages of iron ranging from Fe^{+8} to Fe^{+15} were detected. These high ion stages are in the range that might be expected based upon the *ROSAT* PSPC X-ray observations of the star. The line strengths were weaker than we would have predicted from a one or two temperature component fit to the *ROSAT* data. We explained this as resulting from two effects: there is a distribution in the temperatures in the gas producing the X-ray and EUV iron line emission; and there must be some attenuation of the line emission by the highly ionized material lying between the line source and the Earth. Some of this additional attenuation may be due to the hot, ionized component of the interstellar medium, but much of it should be due to the stellar wind material which lies above the hot, line emitting regions. This analysis is providing new information about the conditions in the wind which could not have been derived from X-ray observations alone.

The strongest emission lines in the spectrum were resonance lines of He II at 304 Å and O III at 374 Å. We considered several possible causes of the 304 Å helium Lyman-α line. It could not be explained from a non-LTE model as arising from the recombination in the upper levels of the photosphere. The model photosphere predicted that the line should not be present because of the extremely low abundance of fully ionized He at small mass depth. The line would also not be produced in the wind if the wind has a temperature in radiative equilibrium with the photosphere, again because there would be too little He^{++}. However, after accounting for the X-rays that are known from *ROSAT* observations to be present in the wind, there is sufficient production of the 304 Å line. The model used for this calculation assumed the X-rays arise from shocks distributed throughout the wind. The optical depth in the 304 Å line was estimated to be of order 10^4. The appearance of the O III 374 Å line strongly in emission was a surprise. It appears to arise primarily because of the 304 Å resonance that is the basis of the well-known Bowen fluorescence mechanism. A second resonance could in principle lead to the pumping of N III and to emission at 452 Å, but this line could not be detected because of the strong continuum emission that is present at this wavelength.

There is an extremely interesting sequence of events occurring in the outer atmosphere of ϵ CMa as revealed by the *EUVE* observations. The photospheric radiation field produces a wind because of line opacity in the atmosphere, some of these lines (e.g., of O IV and O V) we can isolate from within the *EUVE* spectrum, some (e.g, Fe IV) are in thick blends of lines. The wind, which seems to have a mass-loss rate near $1 \times 10^{-8}\ M_\odot\ \mathrm{yr}^{-1}$ contains shocks that arise from line driven instabilities. The shock-heated gas, which may comprise only a small fraction of the wind, produces X-rays that are observed by *ROSAT*. Most of the shock emission is in the form of lines. The *EUVE* spectrum shows at least four of these lines, arising from high ion stages of iron. The X-rays ($E > 54$ eV) and line emission lead to the double ionization of helium, and subsequently to recombination to the $n = 2$ level of He^+, from which the 304 Å Lyman α line is formed. The *EUVE* spectrum shows some of this line radiation that escapes after a large number of resonance scatterings ($\tau \sim 10^4$). During the scattering process O III is pumped and the line at 374 Å results, and because of the fortunate circumstance that the continuum is not large at this wavelength the *EUVE* spectrum shows this line as well.

There are several projects and calculations that are currently underway. We will be obtaining an additional 150,000 seconds of effective observing time on ϵ CMa; this time using the dithering technique, which will greatly reduce the fixed pattern noise that was a problem in the current study. The effects of the EUV radiation from ϵ CMa on the local interstellar cloud in which the Sun is embedded are being explored. Comparisons among various model atmospheres to study the cause for the discrepancy between the observed and predicted EUV spectrum of ϵ CMa are underway. Further analysis of the wind of ϵ CMa will be undertaken. Combining the *EUVE* observations with *ASCA* as well as *ROSAT* observations will be done in order to study the origins of the high temperature gas.

We have had useful discussions on the topics in this paper with Wayne Waldron, Derck Massa, Ping Wang, Rens Waters, Henry Lamers, Rolf Kudritzki and Sally Heap. We also thank Don Lindler for providing the IDL automatic line identification routines. This research was supported in part from an *EUVE* observing grant from NASA, NAGW 5-2282. The work by I. H. and T. L. was supported in part by NASA grants NAGW-3025 and NAGW-3834.

REFERENCES

Abbott, D. C. 1982, ApJ, 259, 282
Abbott, M. J., & Friend, D. B. 1989, ApJ, 345, 505
Anderson, L. S. 1985, ApJ, 298, 848
Auer, L. H., & Mihalas, D. 1969, ApJ, 158, 641
Blackwell, D. E., & Shallis, M. J. 1977, MNRAS, 180, 177
Bohlin, R. C., Savage, B. D., & Drake, J. F. 1978, ApJ, 224, 132
Bowen, I. S. 1935, ApJ, 81, 1
Bowyer, S., & Malina, R. F. 1991, in Extreme Ultraviolet Astronomy, ed. R. F. Malina & S. Bowyer (New York: Pergamon), 397
Bruhweiler, F. C., & Cheng, K.-P. 1988, ApJ, 335, 188
Cassinelli, J. P., MacFarlane, J. J., Welsh, B. Y., Vallerga, J. V., & Vedder, P. W. 1991, in Extreme Ultraviolet Astronomy, ed. R. F. Malina & S. Bowyer (New York: Pergamon), 153
Castor, J. I., & Lamers, H. J. G. L. M. 1979, ApJS, 39, 481
Cheng, K.-P., & Bruhweiler, F. C. 1990, ApJ, 335, 188
Code, A. D., Davis, J., Bless, R. C., & Hanbury Brown, R. 1976, ApJ, 203, 417
Code, A. D., & Meade, M. R. 1979, ApJS, 39, 195
Cohen, M., Walker, R. G., Barlow, M. J., & Deacon, J. R. 1992, AJ, 104, 1650
Cooper, R. G. 1994, Ph.D. thesis, Univ. Delaware
Deguchi, S. 1985, ApJ, 291, 492
Drew, J. E., Denby, M., & Hoare, M. G. 1994, MNRAS, 266, 917
Dupree, A. K., Brickhouse, N. S., Doschek, G. A., Green, J. C., & Raymond, J. C. 1993, ApJ, 418, L41
Eastman, R. G., & MacAlpine, G. M. 1985, ApJ, 299, 785
Gry, C., York, D. G., & Vidal-Madjar, A. 1985, ApJ, 296, 593
Hanbury Brown, R., Davis, J., & Allen, L. R. 1974, MNRAS, 167, 121
Hoare, M. G., Drew, J. E., & Denby, M. 1993, MNRAS, 262, L19
Hoffliet, D., & Jaschek, C. 1982, Bright Star Catalog (New Haven: University Press)
Hubeny, I. 1988, Comput. Phys. Comm., 52, 103
Hubeny, I., Hummer, D. G., & Lanz, T. 1994, A&A, 282, 151
Hubeny, I., & Lanz, T. 1992, A&A, 262, 501
———. 1994, in preparation
Hubeny, I., Lanz, T., & Jeffery, C. S. 1994, TLUSTY and SYNSPEC: A User's Guide, in press
IRAS Point Source Catalog, Version 2. 1988. Joint IRAS Science Working Group (Washington: GPO)
Jamar, C., Macau-Hercot, D., Monfils, A., Thompson, G. I., Houziaux, L., & Wilson, R. 1976, ESA SR-27, Ultraviolet Bright Star Photometric Catalogue (Noordwijk: ESA)
Johnson, H. L., & Mitchell, R. I. 1975, Rev. Mexicano Astron. Af., 1, 3
Kallman, T., & McCray, R. 1980, ApJ, 242, 615
Kelly, R. L. 1987, J. Phys. Chem. Ref. Data, 16, Supp. no. 1
Klein, R. I., & Castor, J. I. 1978, ApJ, 220, 902
Kudritzki, R. F., Puls, J., Gabler, R., & Schmitt, J. H. M. M. 1991, in Extreme Ultraviolet Astronomy, ed. R. F. Malina & S. Bowyer (New York: Pergamon), 130
Kurucz, R. L. 1979, ApJS, 40, 1
Kurucz, R. L. 1992, in Model Atmospheres for Population Synthesis, ed. B. Barbury & A. Renzini (Dordrecht: Kluwer), 225
Lampton, M., Margon, B., & Bowyer, S. 1976, ApJ, 208, 177
MacFarlane, J. J., Cassinelli, J. P., Welsh, B. Y., Vedder, P. W., & Vallerga, J. V. 1991, ApJ, 380, 564
MacFarlane, J. J., Waldron, W. L., Corcoran, M. F., Wolff, M. J., Wang, P., & Cassinelli, J. P. 1993, ApJ, 419, 813
Maeder, A., & Meynet, G. 1988, A&AS, 76, 411
Malina, R. F., Marshall, H. L., & Antia, B. 1994, AJ, 107, 751
Mihalas, D. 1978, Stellar Atmospheres, 2d ed. (San Francisco: Freeman)
Mihalas, D., Kunasz, P. B., & Hummer, D. C. 1975, ApJ, 202, 465
Pauldrach, A. W. A., & Puls, J. 1990, A&A, 237, 409
Raymond, J. C., & Smith, B. W. 1977, ApJS, 35, 419
Remie, H., & Lamers, H. J. G. L. M. 1982, A&A, 105, 85
Snow, T. P., & Morton, D. C. 1976, ApJS, 32, 429
Springmann, U. W. E., & Pauldrach, A. W. A. 1992, A&A, 262, 515
Uesugi, A., & Fukuda, I. 1982, Revised Catalog of Stellar Rotational Velocities (Kyoto: Kyoto Univ.)
Vallerga, J. V., Sigmund, O. H. W., Vedder, P. W., & Gibson, J. L. 1991, Nucl. Instr. & Meth., 310, 317
Vallerga, J. V., Vedder, P. W., & Welsh, B. Y. 1993, ApJ, 414, L65
Waters, L. B. F. M., Cote, J., & Aumann, H. H. 1987, A&A, 172, 225
Watson, R. D. 1972, ApJS, 24, 167
Welsh, B. Y. 1991, ApJ, 373, 556